ENSO-Induced Teleconnection: Process-Oriented Diagnostics to Assess Rossby Wave Sources and Ambient Flow Properties in Climate Models

H. ANNAMALAI,[a,b] RICHARD B. NEALE,[c] AND JAN HAFNER[a]

[a] *International Pacific Research Center, University of Hawai'i at Mānoa, Honolulu, Hawaii*
[b] *Department of Oceanography, University of Hawai'i at Mānoa, Honolulu, Hawaii*
[c] *National Center for Atmospheric Research, Boulder, Colorado*

(Manuscript received 13 May 2022, in final form 29 November 2022)

ABSTRACT: Climate model fidelity in representing ENSO-induced teleconnection is assessed with process-oriented diagnostics that examine a chain of processes, from equatorial Pacific precipitation to the midlatitude circulation pattern over the Pacific–North American regions. Such processes are rarely addressed during model development. Using an upper-tropospheric divergent level, local vorticity gradient of the ambient zonal flow ($\partial^2\overline{U}/\partial y^2$) and a restoring force for Rossby waves (β_*) are estimated, the equivalent barotropic vorticity equation is solved, and an anomalous Rossby wave source (RWS′) quantified. The analysis is applied to AMIP5 and AMIP6 simulations. For a realistic circulation response representation, the hypothesis that models accurately represent the strength and location of RWS′, and spatial variations in β_* is tested. Compared to AMIP5, in AMIP6 there are clear improvements in representing RWS′ and β_*. To validate the hypothesis, the analysis identifies two metrics: spatially coherent RWS′ in the subtropical North Pacific, and longitudes of negative β_* over the western-central North Pacific. By projecting these metrics in two and three-dimensional views, improvements or degradations in model versions are apparent. If a model's fidelity in representing $\partial^2\overline{U}/\partial y^2$ and RWS′ are compromised, then radiated Rossby waves are reflected more equatorward, resulting in zonally elongated circulation anomalies over the central North Pacific. Thus, during climate model development, applying this analysis frequently will keep a regular check on the fidelity of the modeled response to anomalous El Niño convection in conjunction with changing model ambient flow dependencies. This analysis is intended to form a process-oriented diagnostics package, a community contribution to the NOAA Model Diagnostics Task Force.

SIGNIFICANCE STATEMENT: The seasonal changes in tropical Pacific sea surface temperatures associated with El Niño events can have a significant impact in the atmospheric circulation through the North Pacific and on the annual climate variations over North America. Our skill in predicting these impacts depends critically on the ability of climate models to represent these global-scale connections accurately. We show a number of metrics that describe critical processes along this North Pacific pathway that can be used to examine the progress in climate model skill. In the future, these models could benefit significantly from using these metrics with the end goal of much improved predictions of El Niño–related variability.

KEYWORDS: Rossby waves; Climate models; Diagnostics

1. Introduction

a. Background

During El Niño–Southern Oscillation (ENSO) winters an equivalent barotropic stationary wave train pattern dominates over Pacific and North American region (Horel and Wallace 1981) and this pattern can be interpreted as an external Rossby wave forced by equatorial Pacific heating (Hoskins and Karoly 1981; Held and Kang 1987; Trenberth et al. 1998). Rossby wave generation and propagation provides the basis for many theories of how the tropics influence midlatitudes (Hoskins et al. 1977; Held and Kang 1987; Branstator 1983). A process-oriented diagnostic (POD; Maloney et al. 2019; Annamalai 2020) package that addresses the chain of processes, that is, intermediate between equatorial Pacific heating and the circulation pattern over the Pacific and North American regions that are usually not addressed in model evaluations (Deser et al. 2016), is developed. The POD will help to address this critical model evaluation gap, by quantifying the roles of anomalous upper-tropospheric divergent wind patterns in the generation of stationary Rossby waves, and the zonally and meridionally varying ambient flow properties that determine the horizontal propagation of these waves (e.g., Branstator 1985; Ting and Sardeshmukh 1993; Di Carlo et al. 2022). As part of model evaluation, we apply the POD to a subset of climate models that participated in phases 5 and 6 of the Atmospheric General Circulation Model Intercomparison Project (AMIP). Besides assessing the representation of relevant processes in individual models, improvements or degradations in models that participated in both AMIP5 to AMIP6 versions are identified, and their implications to ENSO-induced teleconnections are discussed.

During El Niño winters, positive sea surface temperature (SST) anomalies along the central-eastern equatorial Pacific (e.g., Rasmusson and Carpenter 1982) favor local enhancement of moist static energy, promoting deep convection and

Corresponding author: H. Annamalai, hanna@hawaii.edu

DOI: 10.1175/JCLI-D-22-0346.1

increasing the release of latent heating throughout the troposphere (see Wallace et al. 1998 for a review). The resultant anomalous vertical velocity and upper-level divergence alters the generation of the horizontal component of atmospheric vorticity (Hoskins et al. 1977; Hoskins and Karoly 1981), giving rise to anomalous Rossby wave sources (RWS′; Sardeshmukh and Hoskins 1988). These RWS′ excite normal modes of the zonally varying ambient flow (Simmons et al. 1983). Kang and Held (1986) and Sardeshmukh and Hoskins (1988) emphasized that at upper-tropospheric levels, the contribution by advection of the climatological meridional gradient in absolute vorticity by the anomalous divergent winds can also lead to a significant RWS′ in westerly wind regions, in which Rossby wave motion is possible. Trenberth et al. (1998) provide a comprehensive review on all aspects of tropical–extratropical interactions. Atmospheric general circulation models (AGCMs) forced with ENSO-related SST anomalies exhibit various levels of success in representing this circulation pattern (Shukla and Wallace 1983; Lau and Nath 1994; Hoerling et al. 1997; Kumar and Hoerling 1997; Hoerling and Kumar 2002; Shukla et al. 2000; Barsugli and Sardeshmukh 2002; Peng and Kumar 2005; Annamalai et al. 2007; Peng et al. 2014; Deser et al. 2016; Li et al. 2020, among others).

During boreal winters, a prominent midlatitude circulation over the Pacific–North American region is the so-called Pacific–North American (PNA) pattern defined by Wallace and Gutzler (1981). One established interpretation is that PNA is an internal mode of the midlatitude circulation (Lau 1981) that is amplified by ENSO (Horel and Wallace 1981; Kumar and Hoerling 1995; Lau and Nath 1994; Hoerling et al. 1997; Hoerling and Kumar 2002; Peng and Kumar 2005; Li et al. 2020), that is, ENSO can create preferred teleconnection response patterns, such as the PNA (Trenberth et al. 1998). An alternative interpretation is based on differences in the position and structures of the upper-level height anomalies, particularly during El Niño (e.g., Lopez and Kirtman 2019). Based on this paradigm, Straus and Shukla (2002) suggest that ENSO does not force PNA. Intriguingly, the height anomalies bear close similarity to traditional PNA during La Niña winters (Fig. 1 in Lopez and Kirtman 2019). In the following subsection, we clarify our approach with reference to the above interpretations.

b. *Present study*

Guided by linear and nonlinear model results available in the literature, we hypothesize that the efficacy of climate models' ENSO-induced teleconnection can be assessed by their fidelity in representing anomalous tropical precipitation and associated upper-level divergence, RWS′, and ambient flow characteristics. To test this hypothesis, we have developed a diagnostics package (section 2). Besides assessing climatological basic flow properties and seasonal anomalous conditions during ENSO winters, the barotropic vorticity equation is solved at mid-to-upper-troposphere levels, and terms contributing to the total RWS′ are quantified. Here, to circumvent coupled models' simulated SST biases cascading into anomalous precipitation and RWS′ characteristics, we focus only on the AMIP-type experiments in which all the participating models are forced by observed SSTs (Gates et al. 1992). This limits the attribution of errors solely to limitations in the representation of atmospheric model processes and their interdependencies. However, the presence of error compensation can make such direct attribution challenging.

The POD is applied to five reanalysis products to assess inherent uncertainties among them, and for the purposes of model assessment, robustness in their results is sought. The reason being that in data sparse regions such as the deep tropics, estimates of diabatic processes are not well constrained by in situ measurements. Then, they depend on the first guess provided by the forecast models that is sensitive to the physical parameterizations employed (Annamalai et al. 1999; Zhang et al. 2008).

Figure 1a shows El Niño winter (DJF) composites of geopotential height anomalies at 200 hPa (HGT200) constructed from ERA5 reanalysis (details are given in section 2). One notes alternating signs in HGT200 that arch from the tropical Pacific poleward to the North Pacific, and then eastward and southward across North America exhibiting a wave train pattern. One clear difference from the traditional PNA pattern of Wallace and Gutzler (1981) is the longitudinal shift of centers (~10°) over North Pacific and North America (boxes 2–4 in Fig. 1a), in agreement with Lopez and Kirtman (2019). Guided by Fig. 1a and following the Wallace and Gutzler (1981) approach, a circulation index termed El Niño–induced circulation index (ENCI) over the Pacific–North America is calculated using standardized HGT200 as $0.25 \times (\mathrm{HGT200_{REG1}} - \mathrm{HGT200_{REG2}} + \mathrm{HGT200_{REG3}} - \mathrm{HGT200_{REG4}})$, and the results are shown for the period 1979–2019 (Fig. 1b). For boreal winters, the traditional PNA index obtained from the Climate Prediction Center (CPC) is also shown (Fig. 1c). Both indices, barring differences in magnitude, show positive (negative) values during warm (cold) phases of ENSO, and the cross-correlation between them is 0.8. Our goal here is not to examine how accurately El Niño forces PNA. Our intention is to assess the model processes that are deemed necessary for the forced midlatitude circulation over the Pacific–North American regions during El Niño winters.

In this model evaluation study, we assess the models' fidelity in accurately representing (i) strength and location of RWS′ that depend on anomalous tropical precipitation and associated divergent flow properties, and climatological vorticity gradients in the subtropical jets, and (ii) local vorticity gradient of the ambient zonal flow ($\partial^2\overline{U}/\partial y^2$) in guiding the propagation of Rossby waves. Of relevance, model biases in precipitation (e.g., Kumar et al. 2005; Annamalai et al. 2007; Deser et al. 2016), upper-level divergence and RWS′ (e.g., Jin and Hoskins 1995), and basic-state flow properties (e.g., Branstator 1985; Palmer and Mansfield 1986; Ting and Sardeshmukh 1993) are all expected to influence ENSO-induced teleconnection (Trenberth et al. 1998; Barsugli and Sardeshmukh 2002).

The remainder of the paper is organized as follows: Section 2 deals with the POD and some details of the AMIP simulations and reanalysis products. In section 3, models' ability in representing equatorial Pacific precipitation (EPP) anomalies to

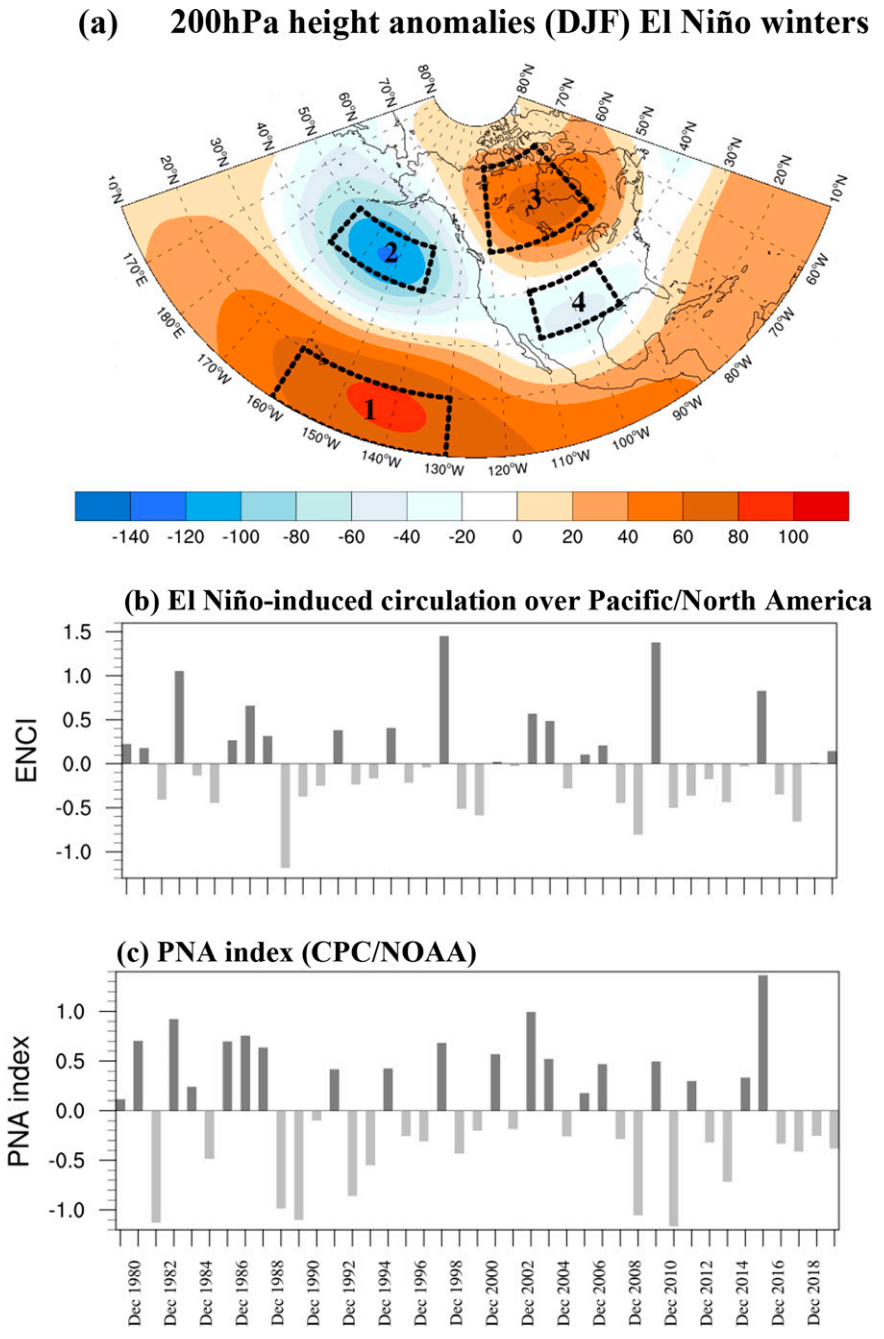

FIG. 1. (a) El Niño winter (DJF) composites of geopotential height (m) anomalies at 200 hPa; (b) boreal winter El Niño–induced circulation index based on four regions [boxed outlines in (a)] for the period 1979–2019 and is calculated as $0.25 \times (\mathrm{HGT200_{REG1}} - \mathrm{HGT200_{REG2}} + \mathrm{HGT200_{REG3}} - \mathrm{HGT200_{REG4}})$ and (c) boreal winter traditional PNA index provided by CPC/NOAA. Results in (a) and (b) are derived from ERA5. Here, REG1 is 10°–20°N, 160°–130°W; REG2 is 40°–50°N, 170°–140°W; REG3 is 50°–70°N, 120°–80°W; and REG4 is 30°–40°N, 110°–90°W.

generation of RWS′ are discussed. Section 4 deals with the models' fidelity in simulating basic-state properties. El Niño–induced teleconnections are interpreted in section 5. In section 6, model biases are quantified, along with improvements or degradations in the transitions from AMIP5 to AMIP6 are shown, and POD's efficiency to model developers along with key implications are presented. Conclusions and future directions are highlighted in section 7. Further discussions on model interpretations on midlatitude circulation are summarized in appendix.

2. ENSO Rossby wave source POD, model solutions and reanalysis products

a. *ENSO_RWS*

The diagnostics package termed ENSO_RWS consists of four levels or steps that are sequentially performed with monthly data either from reanalysis or model integrations. To attain robust composite results a reasonable sample of ENSO winters is needed. However, the POD can be applied even for a single El Niño winter (e.g., seasonal prediction solutions). Similarly, the POD is applicable to any number of pressure levels (e.g., to identify the level at which maximum upper-level divergence and associated RWS′ are located).

In LEVEL 1, monthly anomalies are first constructed. Then, based on a user-defined threshold of ENSO index, ENSO winters are identified and seasonal composites of relevant variables are generated. In LEVEL 2, restoring force for Rossby waves (β_*) is first estimated [Eq. (1)]. Subsequently, stationary wavenumber (K_s) is estimated [Eq. (2)]. Following Hoskins and Ambrizzi (1993), expressions for β_* and K_s are given by

$$\beta_* = \beta - \partial^2\overline{U}/\partial y^2, \tag{1}$$

$$K_s = (\beta_*/\overline{U})^{1/2}, \tag{2}$$

where β ($=df/dy$) is latitudinal variations in planetary vorticity (f), $\overline{U}$ is the basic-state zonal wind velocity, and $\partial^2\overline{U}/\partial y^2$ is the local vorticity gradient of the ambient zonal flow. Stationary Rossby waves are possible if the flow is westerly ($\overline{U}$ positive) and β_* is positive. In the estimation of β_*, the magnitude and curvature of $\overline{U}$ is important, with variations in K_s that subsequently influence the meridional propagation of Rossby waves since waves are always refracted toward latitudes of higher K_s (Hoskins and Ambrizzi 1993).

Level 3 explicitly solves the barotropic vorticity budget for an upper-troposphere level, and the leading terms contributing to the total RWS′ are quantified [Eq. (3)]. Following Sardeshmukh and Hoskins (1988), RWS′ is given by

$$\mathrm{RWS}' = -\bar{\zeta}\nabla\cdot\boldsymbol{v}'_\chi - \boldsymbol{v}'_\chi\cdot\nabla\bar{\zeta} - \zeta'\cdot\nabla\bar{v} - \bar{v}\cdot\nabla\zeta'. \tag{3}$$

Here, ζ and v_χ correspond to absolute vorticity and the divergent component of the wind, respectively. The overbar represents climatological seasonal mean, and the prime refers to seasonal anomalies. The first term in RWS′ corresponds to stretching due to anomalous divergence, and the second term accounts for advection of climatological gradients in ζ by the anomalous divergent wind. The third and fourth terms account for transient eddy convergences of vorticity, and their contributions to RWS′ are small but nonnegligible. Terms in Eq. (3) confirm that RWS′ arises due to details in divergent flow that depends on model's accurately representing tropospheric diabatic processes. Therefore, errors in RWS′ can reflect inherent errors in models' parameterizations and their associated interdependencies.

In level 4, results from levels 1–3 are condensed into scatterplots. Specifically, the sequential plots illustrate the model's ability in representing the chain of processes. The POD is expected to inform the sensitivity of RWS′ to EPP anomalies and ambient flow characteristics and the importance of $\partial^2\overline{U}/\partial y^2$ and β_* in the refraction and reflection properties of Rossby waves.

b. *Model solutions and reanalysis*

The AMIP5/6 suite consists of solutions from a total of 55 models, and the simulation period is 1979–2005 for AMIP5, and 1979–2014 for AMIP6, respectively. Compared to AMIP5, there are additional models in AMIP6 pool (Eyring et al. 2016). The POD is applied to solutions available from all AMIP5/6 models, and results are summarized for AMIP5 and AMIP6 separately as well as for the models that participated in both phases.

To validate model results, similar diagnostics are applied to multiple reanalysis products for the period 1979–2014. We emphasize that reanalysis uncertainties need to be taken into account while validating models. The products we diagnose include the European Centre for Medium-Range Weather Forecasts (ECMWF) interim reanalysis (ERAi; Dee et al. 2011); the fifth major global reanalysis produced by ECMWF (ERA5; Herbasch et al. 2020); the Modern-Era Retrospective Analysis for Research and Applications, version 2 (MERRA-2; Gelaro et al. 2017); the Japanese 55-year Reanalysis (JRA-55; Kobayashi et al. 2015); and the Climate Forecast System reanalysis (CFS-R; Saha et al. 2010).

For models and reanalysis, variables diagnosed include precipitation, three-dimensional winds and geopotential height. All the diagnostics are performed for composite El Niño winters [years when Niño-3.4 (5°S–5°N, 120°–170°W) SST anomalies exceed 1.0 standard deviation]. Since observed SST is prescribed in AMIP simulations, El Niño winters are identical in both reanalysis and models, and thus offer direct comparisons. Due to space constraints, however, spatial plots from only two reanalysis, CFS-R and ERAi, are shown, since in most of the diagnostics presented here, results from these two reanalyses show lower/upper bounds on the five reanalyses considered.

3. Anomalous Rossby wave sources during El Niño winters

First, we assess anomalous tropical precipitation and associated upper-level circulation since model biases in them (e.g., Kumar et al. 2005) modulate the generation of the horizontal component of atmospheric vorticity giving rise to RWS′ (e.g., Jin and Hoskins 1995; Ting and Sardeshmukh 1993). Second, RWS′ spatial patterns in the subtropical North Pacific are discussed. To condense all the results from all the models, scatterplots are shown. In them, vertical and horizontal dashed lines correspond to reanalysis uncertainties measured as lower and upper bound values among them (e.g., Figs. 4, 7 and 13), and a model simulation is interpreted to be realistic if its values fall within these uncertainties. Discussions on the quantification of model biases, and improvements/degradations from AMIP5 to AMIP6 are deferred to section 6.

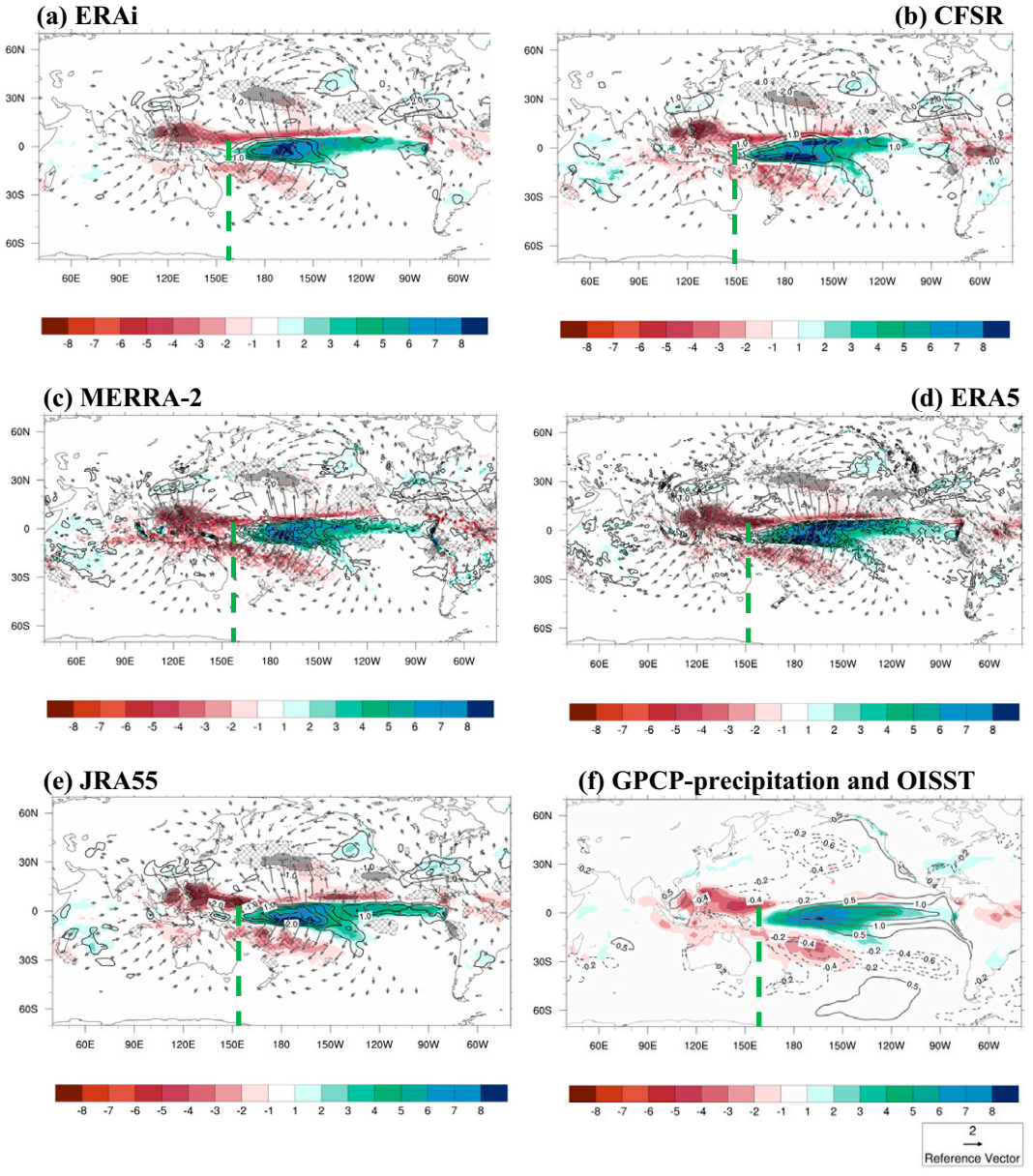

FIG. 2. (a)–(e) El Niño winter (DJF) composites of anomalous precipitation (shaded; mm day^{-1}), 200-hPa convergence/divergence (hatching/contours; 10^{-6} s^{-1}) and 200-hPa divergent winds (m s^{-1}; reference vector is shown) constructed from reanalysis products: (a) ERAi, (b) CFSR, (c) MERRA2, (d) ERA5, and (e) JRA55. (f) Composites of observed precipitation from GPCP and SST anomalies (contours with an interval of 0.5°C for positive and 0.2°C for negative values) are shown. Observed SST is taken from Optimum Interpolated SST products. Green vertical lines correspond to westward extension of positive precipitation anomalies (longitudinal position of 1.0 mm day^{-1} contour) along the equatorial Pacific.

a. El Niño–related precipitation and circulation anomalies at 200 hPa

Figures 2a–e show anomalous precipitation (shaded), 200-hPa divergence/convergence (contours/hatching) and divergent winds (vector) from reanalyses. Observations (Fig. 2f) show that in response to warm SST anomalies (contours) along the central and eastern equatorial Pacific, precipitation (shaded) is increased with a local maximum around the date line (10°S–0°, 160°E–140°W), termed the EPP region. Besides differences in intensity, all the reanalyses represent the EPP pattern. In response to increased convection, locally concentrated anomalous upper-level divergence and divergent winds are seen. Poleward, the meridional component of the divergent wind anomalies converges over the subtropical North Pacific (STNP; 25°–40°N, 150°E–160°W) and along the South Pacific convergence zone, implying a strengthened local overturning Hadley

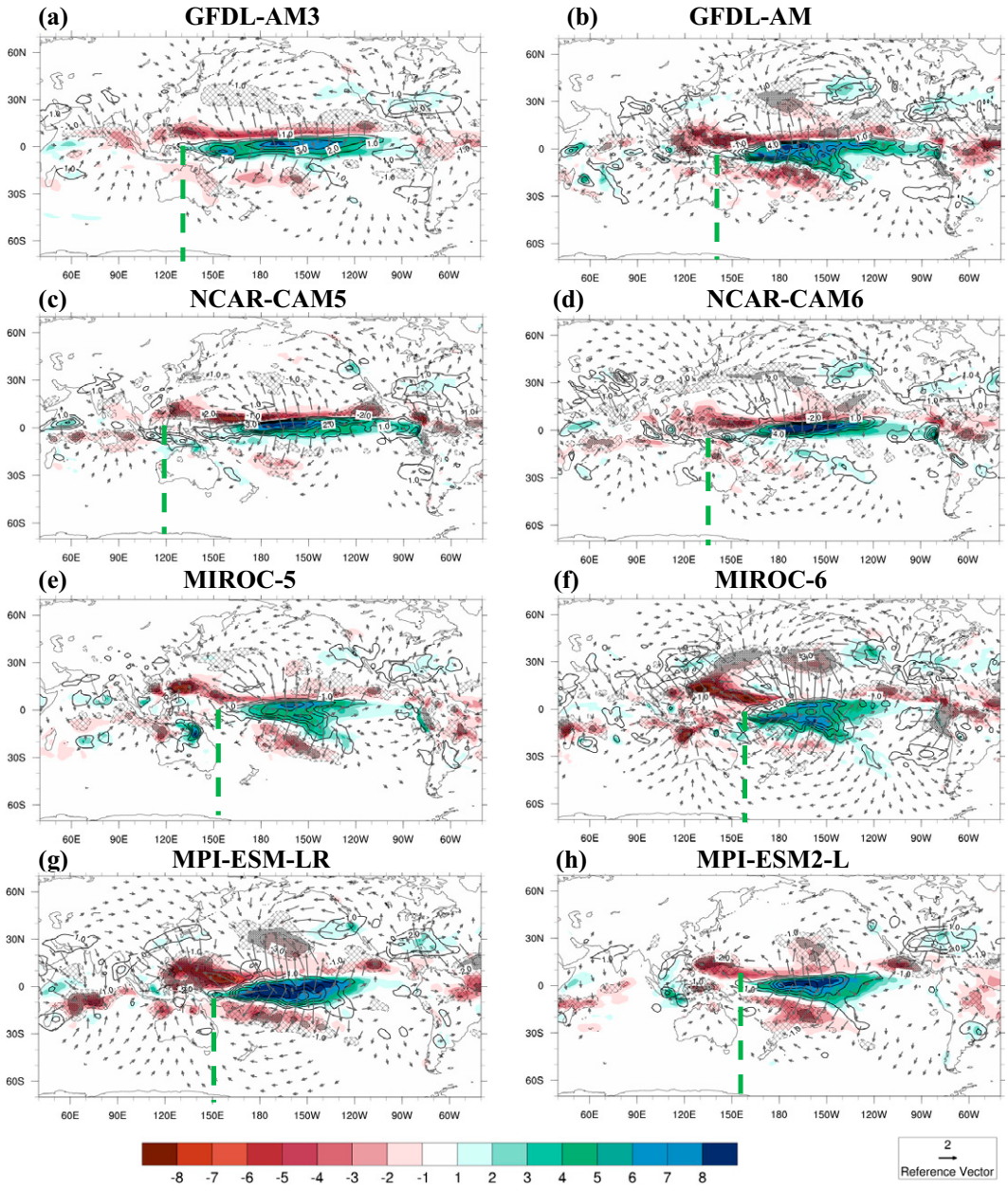

FIG. 3. El Niño winter (DJF) composites of anomalous precipitation (shaded; mm day^{-1}), 200-hPa convergence/divergence (hatching/contours in units of 10^{-6} s^{-1}), and 200-hPa divergent winds (m s^{-1}) constructed from a few models: (left) AMIP5 and (right)AMIP6. Green vertical lines correspond to westward extension of positive precipitation anomalies (longitudinal position of + 1.0 mm day^{-1} contour) along the equatorial Pacific.

circulation. In the equatorial plane, zonal weakening of the Walker circulation with enhanced precipitation over the EPP and suppressed precipitation over the Maritime Continent–tropical western Pacific (MC-TWP), resulting in convergence anomalies over MC-TWP are also apparent. Thus, two well-separated upper-level convergence anomalies, one over the STNP and another over the MC-TWP are evident. In the reanalyses, while the structures of divergent wind anomalies are in good agreement, their intensities differ, which is consistent with the varying precipitation anomalies. Note that a direct comparison of divergent winds in reanalyses will depend on the first guess supplied by the forecast models (Dee et al. 2011). This is sensitive to the physical parameterizations used in each reanalysis model (Annamalai et al. 1999).

Figure 3 shows results from select AMIP5 (left) and their corresponding AMIP6 (right) models while Fig. 4 summarizes all AMIP models' fidelity in capturing anomalous precipitation and STNP convergence. Compared to observations (Fig. 2f),

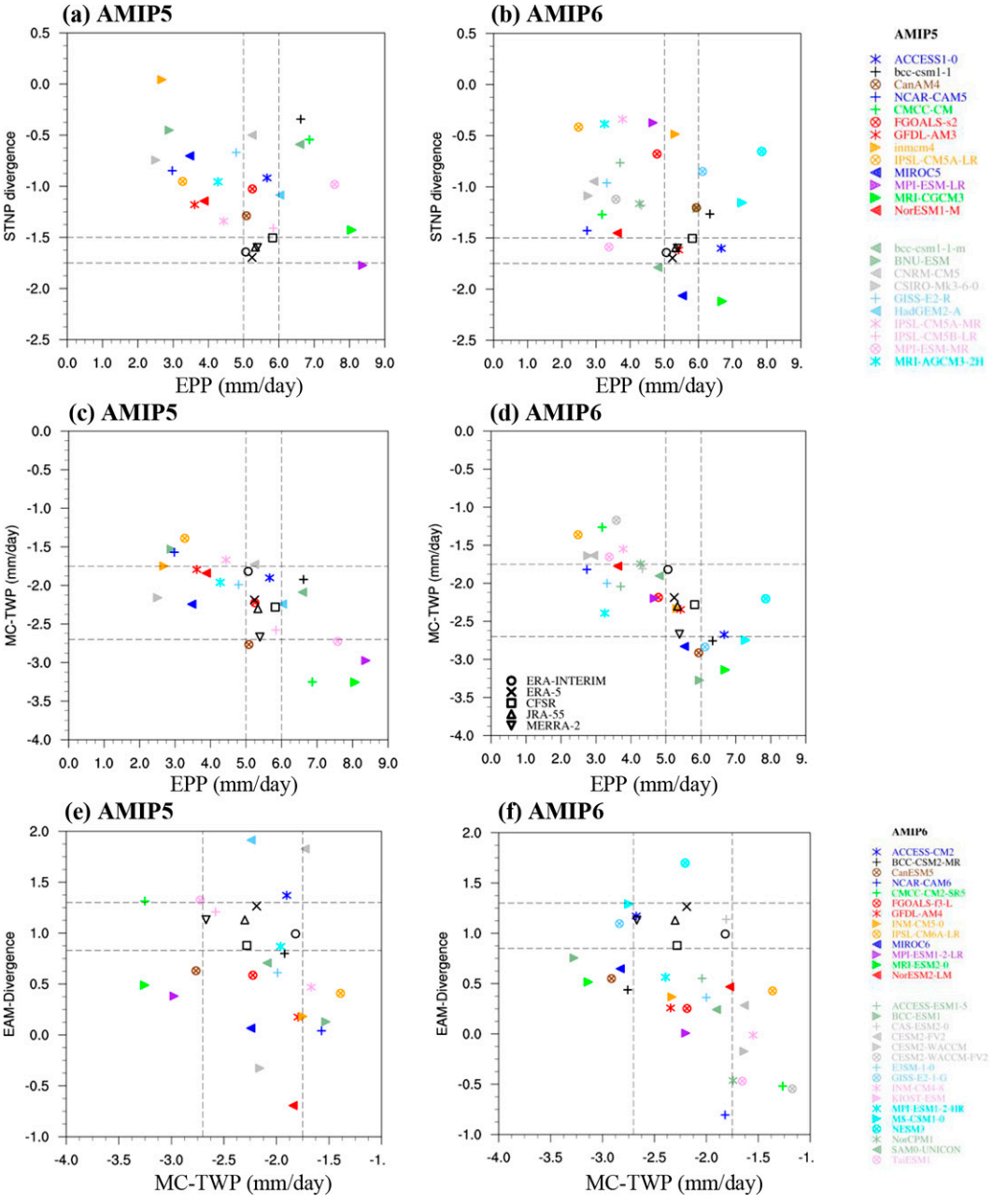

FIG. 4. Scatterplots between simulated anomalous precipitation (mm day^{-1}) averaged over the EPP (10°S–0°, 160°E–140°W) and 200-hPa divergence (10^{-6} s^{-1}) averaged over the STNP (25°–40°N, 150°E–160°W): (a) AMIP5 models; (b) AMIP6 models. (c),(d) As in (a) and (b), but for EPP and precipitation anomalies averaged over MC-TWP (5°S–18°N, 110°–150°E). (e),(f) As in (a) and (b), but for MC-TWP precipitation and 200-hPa divergence (10^{-6} s^{-1}) averaged over the EAM region (20°–30°N, 100°–140°E). The vertical and horizontal dashed lines correspond to reanalysis uncertainties measured as lower and upper bound values among them, and a model simulation is interpreted to be realistic if its values fall within these uncertainties.

both in GFDL-AM3 (Fig. 3a) and CAM5 (Fig. 3c), EPP anomalies are *meridionally confined but zonally elongated*, extending well into the western equatorial Pacific (green vertical lines) with implications for westward shifts in anomalous convergence in the STNP. Also, suppressed precipitation and convergence anomalies protrude into the eastern equatorial Indian Ocean. In contrast, EPP anomalies in MIROC5 and MPI-ESM-LR are stronger than observations (Fig. 4c), but STNP convergence anomalies are stronger in MPI-ESM-LR (Fig. 4a) while they are unorganized with multiple local maxima in MIROC5 (Fig. 3e).

In GFDL-AM4 (Fig. 3b) and CAM6 (Fig. 3d), notable improvements include a reduced westward extension of EPP anomalies and spatially organized convergence anomalies in the STNP. Based on EPP and MC-TWP precipitation anomalies (Figs. 3b,d and 4d), the anomalous Walker circulation is realistic in GFDL-AM4 while both precipitation anomalies are weaker than observations in CAM6. The reduced precipitation anomalies protruding into the eastern equatorial Indian Ocean still persist from CAM5, and a narrow tongue of unrealistic convergence anomalies extends along the subtropical Asian jet (around 30°N). This is a feature present in all CAM6 model versions including Finite Volume 2 degree resolution (FV2), WACCM, and WACCM-FV2 (not shown). Compared to MIROC5 (Fig. 3e), considerable improvements in MIROC6 (Fig. 3f) include STNP convergence and positive precipitation anomalies along the East Asian monsoon (EAM; 20°–30°N, 100°–140°E). Of all the AMIP5 models, anomalous EPP and STNP convergence are by far the strongest in MPI-ESM-LR (Fig. 4a), while they are weaker in its AMIP6 version (Fig. 4b).

Scatterplots (Fig. 4) summarize models' abilities in representing anomalous local Hadley (Figs. 4a,b) and planetary Walker (Figs. 4c,d) circulations. Compared to reanalysis, simulated anomalous tropical precipitation and associated upper-level circulation in most models are weaker. The intermodel spreads between EPP (~2.5 to 8.0 mm day^{-1}) and STNP convergence (0 to -2.2×10^{-6} s^{-1}), as well as a varied convergence response for similar EPP forcing and vice versa are readily apparent (Figs. 4a,b). The strong association (both in sign and amplitude) between the EPP wetness and MC-TWP dryness (Figs. 4c,d) can be interpreted as follows: The anomalous Walker circulation with ascent over the equatorial central-eastern Pacific leads to descent and low-level divergence over the MC-TWP. Subsequently, the low-level anomalous westerlies advect climatological moisture from the equatorial west to central Pacific further feeding the convection and enhancing ascent (Annamalai 2020). Figures 4e and 4f summarizes the linkage between MC-TWP dryness and regional divergence anomalies along the EAM front. The low-level anomalous anticyclonic circulation that develops in response to reduced MC-TWP precipitation, through horizontal moist advection, leads to a strengthened EAM and, hence, upper-level divergence (e.g., Annamalai et al. 2005). However, large scatter between MC-TWP dryness and EAM-divergence may be attributed to models' inability in representing latitudinally confined EAM anomalous precipitation (Figs. 2 and 3). Within reanalysis uncertainties, it must be emphasized that GFDL-AM4 captures realistic simulations of both anomalous EPP and STNP convergence (Fig. 4b), and MC-TWP dryness (Fig. 4d). As will be shown next, both convergence over the STNP and divergent wind anomalies along the EAM contribute to $-\bar{\zeta}\nabla\cdot v'_\chi$ and $-v'_\chi\cdot\nabla\bar{\zeta}$ terms of RWS′, respectively.

b. Anomalous Rossby wave sources at 200 hPa

Figures 5 and 6 show the geographical distributions of RWS′ (shading) from two reanalysis (Figs. 5a and 6a) and a selection of AMIP5 (Figs. 5b–e) and AMIP6 (Figs. 6b–e) models. In the right panels, 200-hPa climatological $\bar{\zeta}$ (contours), v'_χ and total RWS′ (shaded) are shown. Note that the left and center panels have different shading scale. In both reanalyses, compared to subtropics, values of RWS′ are smaller in the deep tropics owing to smallness in $\bar{\zeta}$. Elsewhere, the contribution due to the vortex stretching term ($-\bar{\zeta}\nabla\cdot v'_\chi$) dominates the total RWS′ (right panels). Combining earlier results (Figs. 2–4), anomalous convergence over the STNP determines the stretching dominance, resulting in a cyclonic vorticity source. This will be termed the primary RWS′. Note that the primary source is situated in the climatological large-scale trough region (right panels), and this favors Rossby wave rays to be directed more toward the pole (Branstator 1983). v'_χ is perpendicularly oriented to the $\bar{\zeta}$ contours and determines the zonal structure and sign of $-v'_\chi\cdot\nabla\bar{\zeta}$ (middle panels) and its contribution with a local maximum along the Asian jet is important for accurate representation of RWS′ over 25°–40°N, 80°E–170°W. Contributions from transient eddy convergence of vorticity [last two terms in Eq. (3)] to RWS′ are small and hence not shown.

In GFDL-AM3, the STNP maxima in $-\bar{\zeta}\nabla\cdot v'_\chi$ is weak and located west of the date line. Along the Asian jet the tongue of positive vorticity due to $-v'_\chi\cdot\nabla\bar{\zeta}$ is also shifted west. Both are factors attributed to errors in representing perturbations to the local Hadley and planetary Walker circulations as implied in the divergent winds (right panels in Figs. 5 and 6). These limitations are seemingly overcome in GFDL-AM4 (Fig. 6b). Similarly, compared to CAM5, there is a clear improvement in the representation of the primary RWS′ in CAM6; however, the westward extension of zonally elongated signatures in both $-\bar{\zeta}\nabla\cdot v'_\chi$ and $-v'_\chi\cdot\nabla\bar{\zeta}$ along the Asian jet (Fig. 6c) reflect the need for further model improvements. Compared to its AMIP5 counterpart (Fig. 5d), components of RWS′ are similarly better represented in MIROC6 (Fig. 6d). Of all the AMIP6 models, amplitudes of both $-\bar{\zeta}\nabla\cdot v'_\chi$ and $-v'_\chi\cdot\nabla\bar{\zeta}$ are the strongest in MIROC6, resulting in a too-strong RWS′ over the STNP (Figs. 7c,d). In contrast, realistic representations of RWS′ in MPI-ESM-LR (Fig. 5e) are degraded in its AMIP6 version (Fig. 6e).

To assess the role of simulated biases in anomalous precipitation, divergence, and climatological $\bar{\zeta}$ and its gradient in representing leading RWS′ in models, we show scatterplots among these variables (Fig. 7). While there is considerable model scatter between simulated anomalous EPP and STNP convergence (Fig. 4), the subsequent relationship of STNP divergence on the primary RWS′ is largely linear for most models. The diverse response in $-\bar{\zeta}\nabla\cdot v'_\chi$ in AMIP6 for divergence anomalies around ~−1.25 (Fig. 7c), and −0.7 in AMIP5 (Fig. 7a) is perhaps due to diversity in models' climatological relative vorticity averaged over the STNP (not shown). Representing anomalous positive precipitation along the EAM front and associated divergent winds that determine $-v'_\chi\cdot\nabla\bar{\zeta}$ are indeed difficult. This is in large part due to existing precipitation biases in models, but also due to how models relate precipitation anomalies to circulation anomalies given the vertical profile of heating is key to this connection. Even in reanalyses (Fig. 7d; note the spread in precipitation anomalies from 0.7 to 1.2 mm day^{-1} for $-v'_\chi\cdot\nabla\bar{\zeta}$

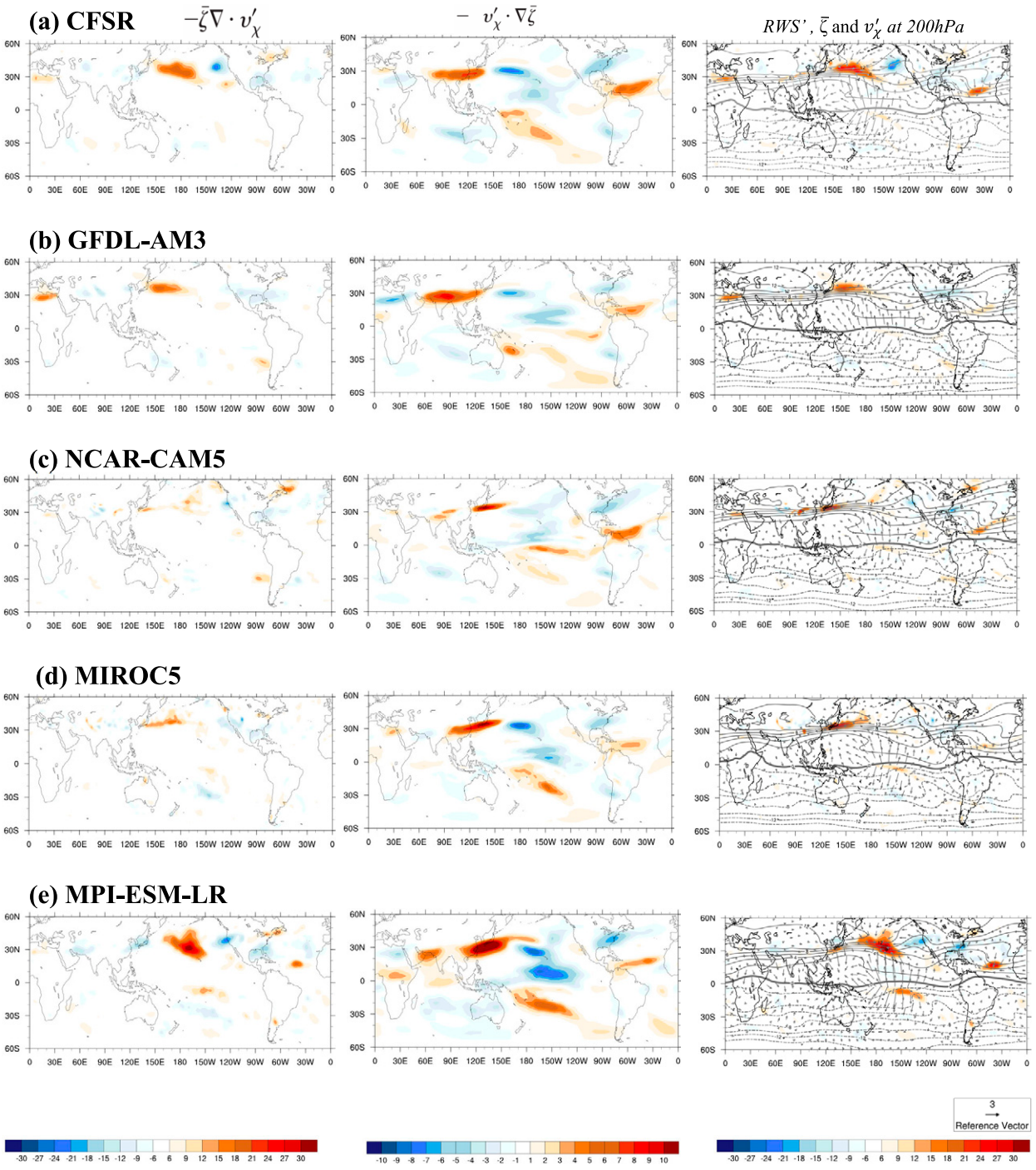

FIG. 5. 200-hPa anomalous Rossby wave source (10^{-11} s^{-2}; shading) due to (left) stretching term, (center) advection term, and (right) total from (a) CFSR, (b) AM3, (c) CAM5, (d) MIROC5, and (e) MPI-ESM-LR. Results from a few select AMIP5 models are shown. In the right panels, 200-hPa climatological absolute vorticity (10^{-5} s^{-1}; contours with an interval of 2×10^{-5} s^{-1} and zero contour as thick) and anomalous divergent winds (m s^{-1}) are also shown. Reference vector is shown. Note that the center column has a different shading scale.

values ~5.0×10^{-11} s^{-2}) the relationship is poorly constrained. Reanalyses results suggest that contributions from $-v'_\chi \cdot \nabla\bar{\zeta}$ lie in the range of 4.5–5.5 $\times 10^{-11}$ s^{-2} while that of $-\bar{\zeta}\nabla \cdot v'_\chi$ is 11–13 $\times 10^{-11}$ s^{-2}. In both AMIP versions, large scatters and ranges in both $-\bar{\zeta}\nabla \cdot v'_\chi$ and $-v'_\chi \cdot \nabla\bar{\zeta}$ imply errors in divergent flow properties that depend on models' accurately representing tropospheric diabatic processes. Compared to their AMIP5 counterparts, many models (GFDL-AM4,

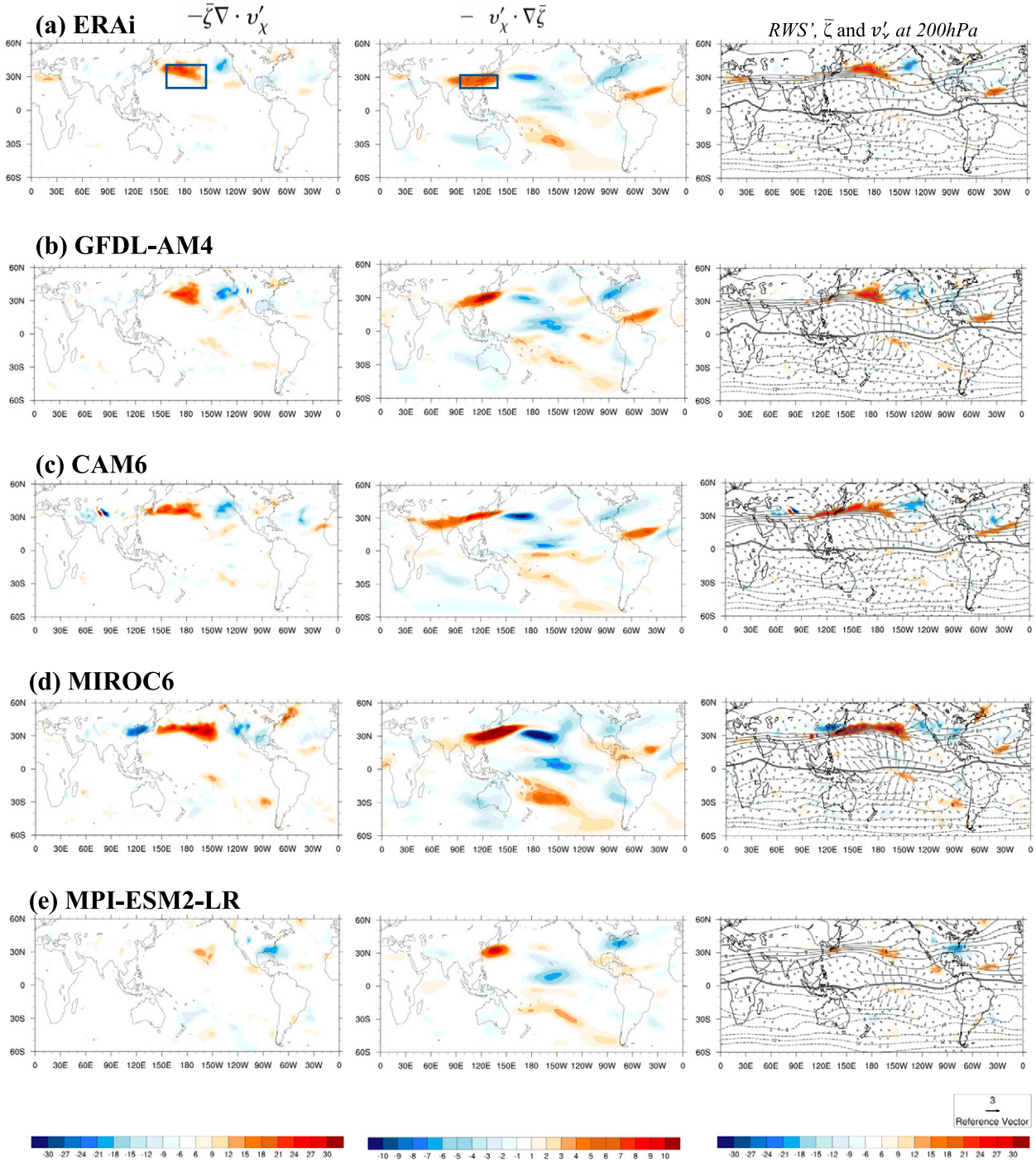

FIG. 6. 200-hPa anomalous Rossby wave source (10^{-11} s^{-2}; shading) due to (left) stretching term, (center) advection term, and (right) total from (a) ERAi, (b) GFDL-AM4, (c) CAM6, (d) MIROC6, and (e) MPI-ESM2-LR. Results from a few select AMIP6 models are shown. In the right panels, 200-hPa climatological absolute vorticity (10^{-5} s^{-1}; contours with an interval of 2×10^{-5} s^{-1} and zero contour as thick) and anomalous divergent winds (m s^{-1}) are also shown. Reference vector is shown. Note that the center column has a different shading scale. The boxed region in the top-left (top-center) panel shows the averaging area used to estimate $-\bar{\zeta}\nabla\cdot v'_\chi$ ($-v'_\chi\cdot\nabla\bar{\zeta}$) for results shown in later figures.

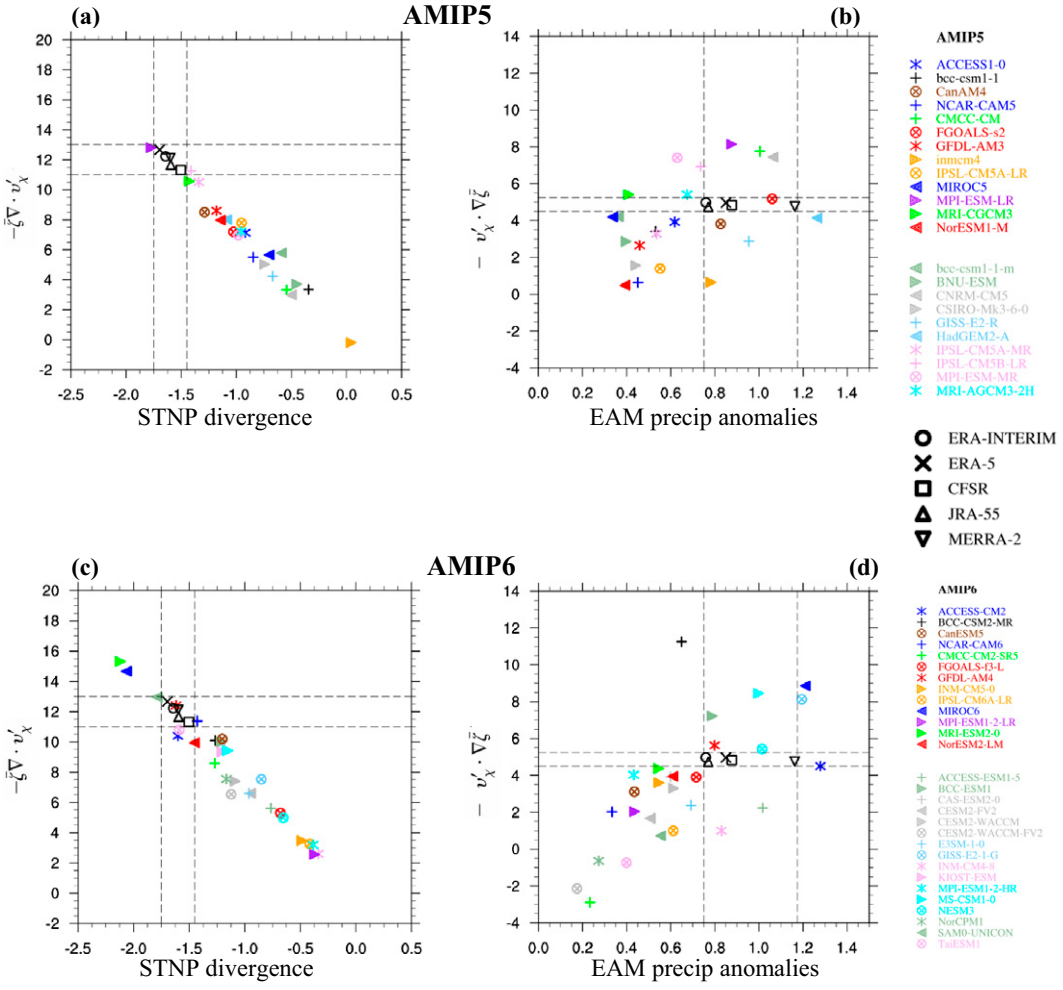

FIG. 7. (left) Scatterplots between simulated anomalous 200-hPa divergence (10^{-6} s^{-1}) averaged over the subtropical North Pacific (25°–40°N, 150°E–160°W) and RWS′ due to stretching term, $-\bar{\zeta}\nabla\cdot v'_\chi$ (10^{-11} s^{-2}); (right) scatterplots between simulated anomalous precipitation (mm day^{-1}) averaged over the East Asian monsoon front (22°–32°N, 110°–140°E) and RWS′ due to advection term, $-v'_\chi\cdot\nabla\bar{\zeta}$ (10^{-11} s^{-2}). (a),(b) All AMIP5 models and (c),(d) all AMIP6 models. The vertical and horizontal dashed lines correspond to reanalysis uncertainties measured as lower and upper bound values among them, and a model simulation is interpreted to be realistic if its values fall within these uncertainties. The averaging areas for $-\bar{\zeta}\nabla\cdot v'_\chi$ and $-v'_\chi\cdot\nabla\bar{\zeta}$ are shown in Fig. 6a.

CAM6, bcc-csm2-mr, MIROC6, NorESM2-LR, CMCC-CM2-SR5) show improvements in $-\bar{\zeta}\nabla\cdot v'_\chi$ in their AMIP6 versions (Fig. 7c). More discussions are provided in section 6 (Figs. 14–16).

In summary, the POD identifies model STNP RWS′ deficiencies as being due to the following:

- Limitations in v'_χ over the STNP highlighting limitations in representing perturbations to the local Hadley circulation, and hence on $-\bar{\zeta}\nabla\cdot v'_\chi$.
- Westward extension of EPP anomalies and associated anomalous convergence, accounting for spatially incoherent and zonally elongated RWS′ along the jet.
- Limitations in representing the structure of $\nabla\bar{\zeta}$ along the Asian jet, and enhanced precipitation along the EAM front, which have implications for RWS′ through contributions from $-v'_\chi\cdot\nabla\bar{\zeta}$.

4. Ambient flow properties at 200 hPa

In this section, we assess models' fidelity in accurately representing climatological flow characteristics since model biases in them influence the propagation of stationary Rossby waves, and subsequently influence ENSO-induced teleconnections (e.g., Branstator 1985; Palmer and Mansfield 1986; Ting and Sardeshmukh 1993). Figure 8 shows 200-hPa climatological flow properties of $\overline{U}$, $\partial^2\overline{U}/\partial y^2$, β_*, and K_s for CFSR and ERAi. Prominent elements in $\overline{U}$ include the African–Asian jet, North American–Atlantic jet, and longitudinally

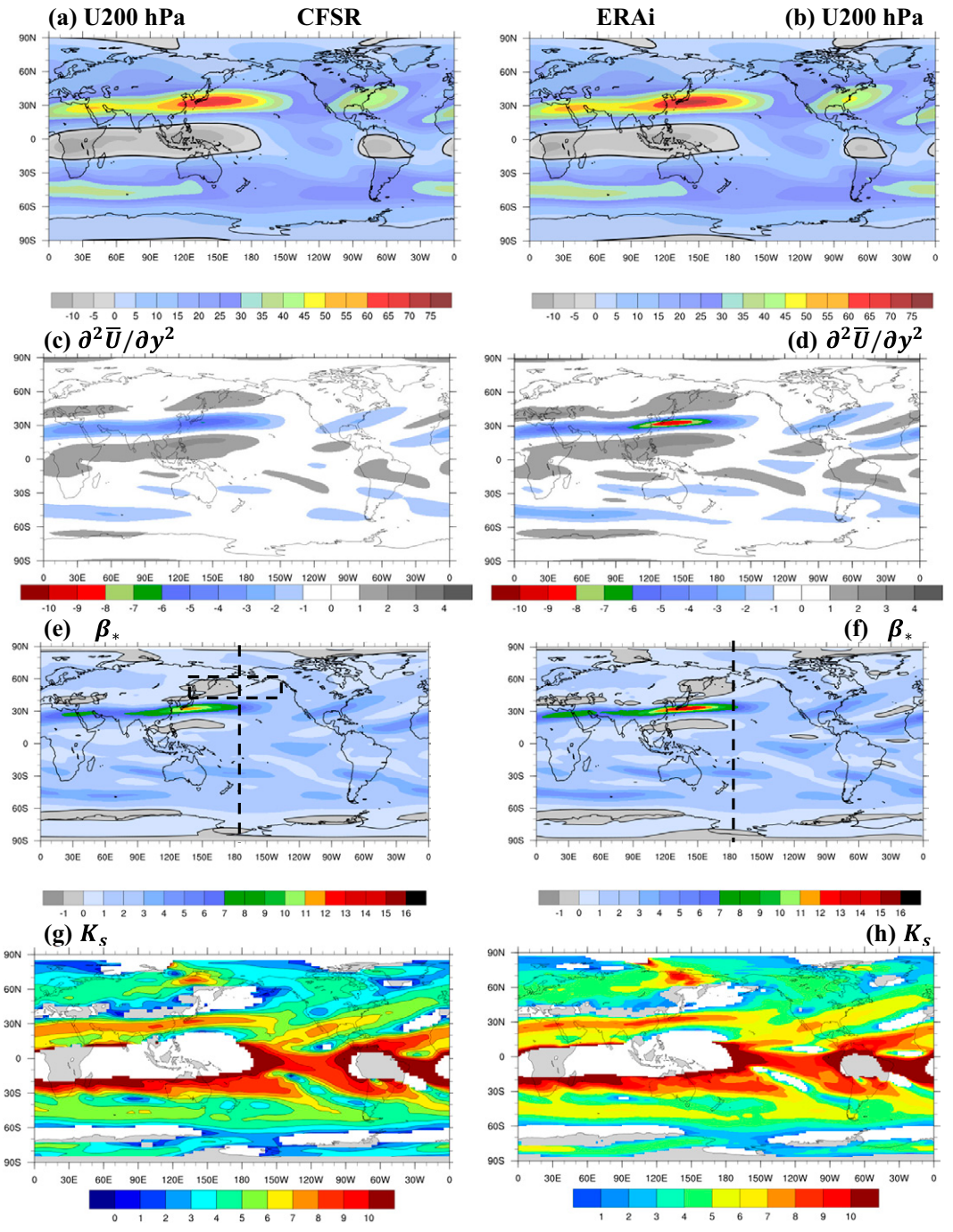

FIG. 8. Boreal winter (DJF) climatological features at 200 hPa from two reanalysis: (a),(b) zonal wind (m s^{-1}); (c),(d) $\partial^2\overline{U}/\partial y^2$ (10^{-11} m^{-1} s^{-1}); (e),(f) β_* (10^{-11} m^{-1} s^{-1}); (g),(h) K_s. (left) CFSR; (right) ERAi. In (a) and (b), easterlies are shown in gray; in (e) and (f), negative values of β_* are shown in gray; and in (g) and (h), undefined values in K_s are shown in white. Boxed outline in (e) corresponds to central North Pacific region (40°–60°N, 130°E–140°W), and vertical dashed lines in (e) and (f) correspond to longitude of zero values of β_* in that region.

extended Southern Hemisphere westerly maxima. Easterlies are prominent over the near-equatorial African–Indian Ocean–MC-TWP and South American regions. Spatial distributions in β_* suggest that a local maximum along the African–Asian jet with weak but negative values to the north of it, and also south of the Asian jet. Importantly, $\partial^2\overline{U}/\partial y^2$ (latitudinal gradient of local relative vorticity of the time-averaged zonal wind) subtracted from β [Eq. (2)] augments the

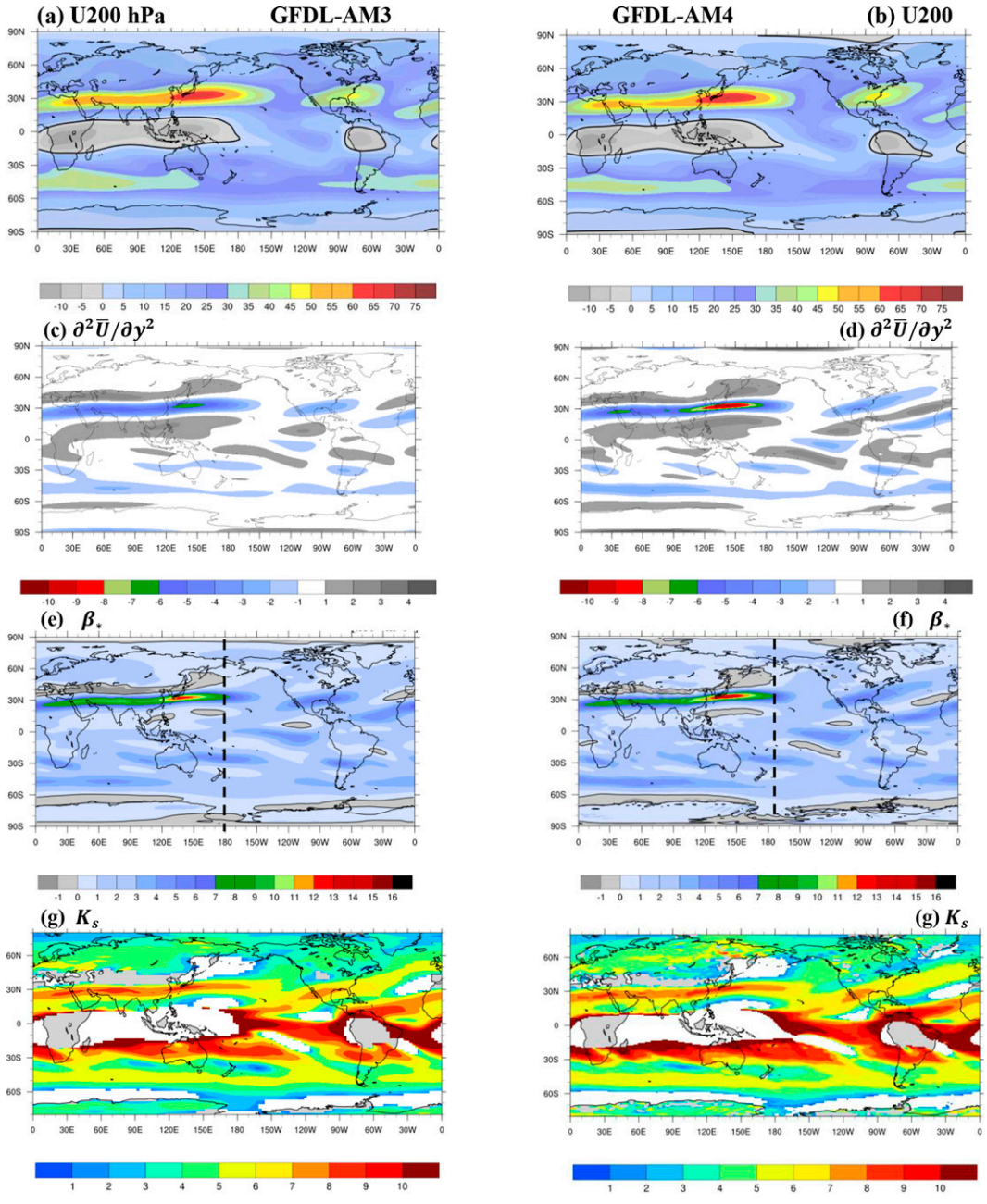

FIG. 9. Boreal winter (DJF) climatological features at 200 hPa from GFDL AM3 and AM4: (a),(b) zonal wind (m s^{-1}); (c),(d) $\partial^2\overline{U}/\partial y^2$ (10^{-11} m^{-1} s^{-1}); (e),(f) β_* (10^{-11} m^{-1} s^{-1}); (g),(h) K_s. (left) GFDL-AM3; (right) GFDL-AM4. In (a) and (b), easterlies are shown in gray; in (e) and (f), negative values of β_* are shown in gray; and in (g) and (h), undefined values in K_s are shown in white. Vertical lines in (e) and (f) correspond to longitude of zero values of β_* in the central-North Pacific (40°–60°N, 130°E–140°W).

concentration of vorticity along the jet (Figs. 8e,f). The spatial distributions in β_* are largely determined by $\partial^2\overline{U}/\partial y^2$ or simply $\overline{U}$. The spatial variations in K_s, diagnose a Rossby waveguide along the African–Asian jet extending over the western-central North Pacific with undefined values in regions of mean easterlies and/or negative values of β_* (e.g., Hoskins and Ambrizzi 1993). Compared to ERAi, $\partial^2\overline{U}/\partial y^2$ in CFSR is weaker along the African–Asian jet resulting in a weaker β_* and K_s along the jet. Interreanalysis differences are also present in MERRA-2, JRA55 and ERA5 (not shown). Thus, disagreement among reanalysis needs to be taken into account while interpreting model results.

To illustrate the challenge of choosing a reanalysis for model validation of high-order dynamical flow properties,

GFDL-AM3 and GFDL-AM4 are compared in Fig. 9. In GFDL-AM3, the spatial variations in $\overline{U}$, $\partial^2\overline{U}/\partial y^2$, β_*, and K_s along the African–Asian jet are in good agreement with CFSR (Fig. 8). In GFDL-AM4, in contrast, spatial variations in the ambient flow properties along, and poleward/equatorward of the African–Asian jet are consistent with ERAi (Fig. 8). Model fidelity in accurately representing spatially coherent negative β_* values over the western-central North Pacific (40°–60°N, 130°E–140°W) depends on accurately representing $\partial^2\overline{U}/\partial y^2$ between the core of the Asian jet (~30°N, 130°E–180°) and western-central North Pacific (~60°N, 130°E–180°). GFDL-AM3 and GFDL-AM4 can both appear realistic, depending on which reanalysis is used. One systematic error in GFDL models (in most AMIP5/6 models too) is that negative values of β_* zonally extend west in Asia just poleward of the African–Asian jet.

5. Circulation response during El Niño winters

In models, we test the hypothesis that realistic simulations of primary RWS′ (Figs. 5–7), $\partial^2\overline{U}/\partial y^2$ and β_* variations (Figs. 8 and 9) *are necessary but not sufficient conditions* for a realistic circulation response over the Pacific–North American regions. Meridional wind anomalies at 200 hPa (V200) serve as a measure of equivalent barotropic stationary Rossby waves, and local maxima of V200 indicate propagation path of these waves. While there may be underlying uncertainty as to whether El Niño forces PNA, here we assess models' ability in representing PNA and ENCI (Figs. 1b,c), and show that at least from the POD employed here, our interpretation does not change. PNA standardized index is estimated from HGT200 (Wallace and Gutzler 1981). To aid in the interpretation of wave propagation, over central North Pacific (40°–60°N, 130°E–140°W) we identify the longitude at which zero values of β_* are located (Figs. 9e,f and 10a–e). A β_*LON is then defined with respect to the date line (positive values refer to east of the date line, and negative values refer to west of the date line in Figs. 13–16).

a. *Circulation response over North Pacific and North America*

Figures 10 and 11 show 200-hPa boreal winter climatological distribution of β_* superimposed on total RWS′ (left panels), along with HGT200 and V200 (right panels). Since the deep tropical circulation response is robust across the models, we show HGT200 poleward of 20°N only. Spatial variations in $\partial^2\overline{U}/\partial y^2$ are shown in Fig. 12. The same was previously shown for GFDL AM3/AM4 in Fig. 9. The observed circulation response comprises centers of alternating signs in HGT200 (e.g., Figs. 10f and 11f) and arches from the tropical Pacific poleward to North Pacific, and then eastward and southward across North America exhibiting a wave train pattern. V200 shows patterns that are in quadrature with HGT200. Based on the above results, we will assess the following:

- The coherent versus diffuse nature of the primary RWS′ region and its location in the STNP (west or east of the date line or zonally elongated along the jet).
- Spatial distributions of $\partial^2\overline{U}/\partial y^2$ and β_* on their impact on reflection/refraction properties of the waves.

Of the AMIP5/6 models, GFDL-AM4 and CAM6 capture the most realistic El Niño–induced circulation anomalies (Figs. 11g,h) with a characteristic meridional propagation from the tropics to North Pacific and then arching northeastwards covering North America, and finally southern parts of the United States of America. Over the north-central Pacific, compared to AMIP5 versions (Figs. 10b,c), there are improvements in representing $\partial^2\overline{U}/\partial y^2$ (Figs. 9, 12) and β_*, and a realistic RWS′ over STNP (Figs. 11b,c, 13c,d), all factors favoring improved midlatitude circulation response over the Pacific–North American region

In many models, a very common erroneous feature is zonally elongated (northwest–southeast oriented) HGT200 over the Aleutian low region. If the primary RWS′ is positioned to the west of the date line (e.g., MIROC5; Fig. 10d) then owing to the presence of positive values in $\partial^2\overline{U}/\partial y^2$ (Fig. 12) or negative values of β_* to the west and poleward of this RWS′, meridional propagation of Rossby waves are not permitted. Therefore, waves generated there will get reflected and become zonally elongated in the east–west direction, as ray tracing theory would suggest (Hoskins and Karoly 1981; Hoskins and Ambrizzi 1993). If the primary RWS′ is diffused (MPI-ESM2-LR; Fig. 6e), and/or if negative values of β_* over central North Pacific extend too eastward (MIROC6; Fig. 11d) HGT200 over the Aleutian low region are weak and zonally elongated as well (Figs. 11i,j). Specifically, instead of pure meridional propagation from the forcing region, both HGT200 and V200 patterns in Figs. 11i and 11j suggests northeast arching wave train indicating reflected waves due to inaccurate ambient flow conditions.

In GFDL-AM3 (Fig. 10b), negative values in β_* are not well defined over the central-North Pacific and thus meridional propagation of Rossby waves forced by RWS′ positioned to the west of the date line is possible. Therefore, we infer waves emanating from west of Japan arch northeastward depict a different propagation path (Fig. 10g). Furthermore, in both GFDL-AM3 and MIROC5 the primary RWS′ reside along the Asian jet (Figs. 10b,d) in which K_s is higher (Fig. 9g), and β_* is strongest (Fig. 9e). Then the radiated waves get trapped along the waveguide and tend to move poleward and equatorward as they exit the jet region. Thus, interference from multiple waves with different wavelengths may contribute to unrealistic circulation anomalies, as implied in barotropic model solutions (Held and Kang 1987). Therefore, in assessing climate models' fidelity to represent PNA or ENCI it is crucial to assess models' ability in accurately representing β_*LON. Ultimately, this metric depends on a model's eastward extension of the Asian jet, and more precisely on $\partial^2\overline{U}/\partial y^2$.

b. *Metrics to assess models' circulation performance*

We identify two metrics, namely, RWS′ and β_*LON, and to assess models' PNA/ENCI dependence on either of them, scatterplots are shown in Fig. 13. Results from AMIP5 (AMIP6) are shown in the top (middle) panels for

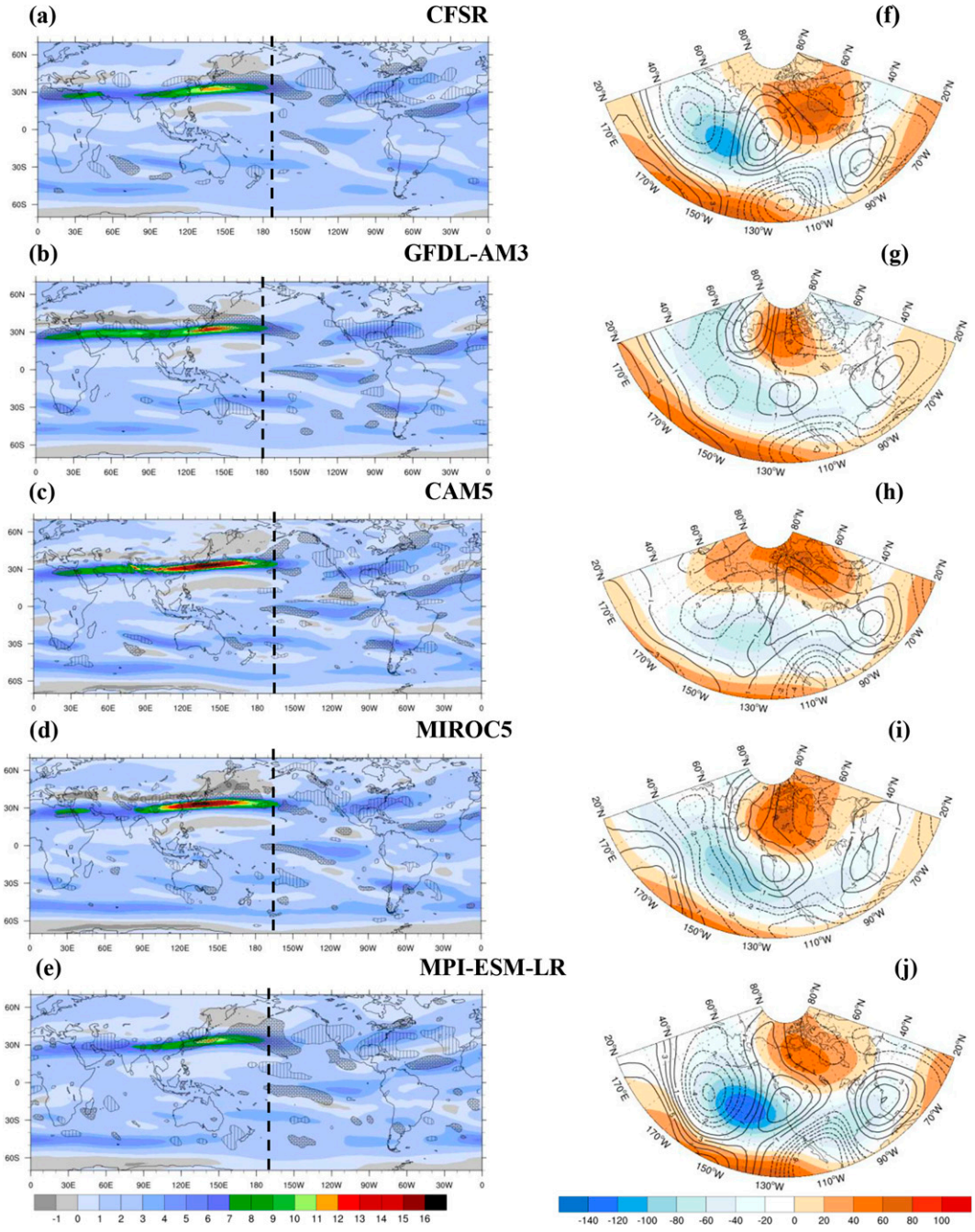

FIG. 10. 200-hPa boreal winter (DJF): (left) climatological β_* (shading; 10^{-11} m^{-1} s^{-1}) and RWS′ (dark hatching for positive values and light hatching for negative values; 10^{-11} s^{-2}); (right) 200-hPa geopotential height (shaded; m) and meridional wind (contours; m s^{-1}) anomalies during El Niño. Vertical lines in the left column correspond to longitude of zero values of β_* in North Pacific. Results from CFSR and a few AMIP5 models are shown.

PNA, and only AMIP6 for ENCI are shown in the bottom panels. In the left panels, 0 in β_*LON refers to the date line. In both metrics, there are clear uncertainties among reanalyses, and assessing the models within these uncertainties suggests that there is a clear improvement in AMIP6, that is, the number of models with realistic PNA/ENCI or RWS′ is higher compared to AMIP5. For both circulation indices, similar response for diverse RWS′ and varied response for similar RWS′, and similar diversity in β_*LON and PNA/ENCI are common. Even if the two metrics are realistic, simulated PNA/ENCI can be either stronger (e.g., GFDL-AM4 and CAM6) or weaker [e.g., Taiwan Earth System Model, version 1 (TaiESM1) and Meteorological Sciences Community System Model 1-0 (MS-CSM-1-0)].

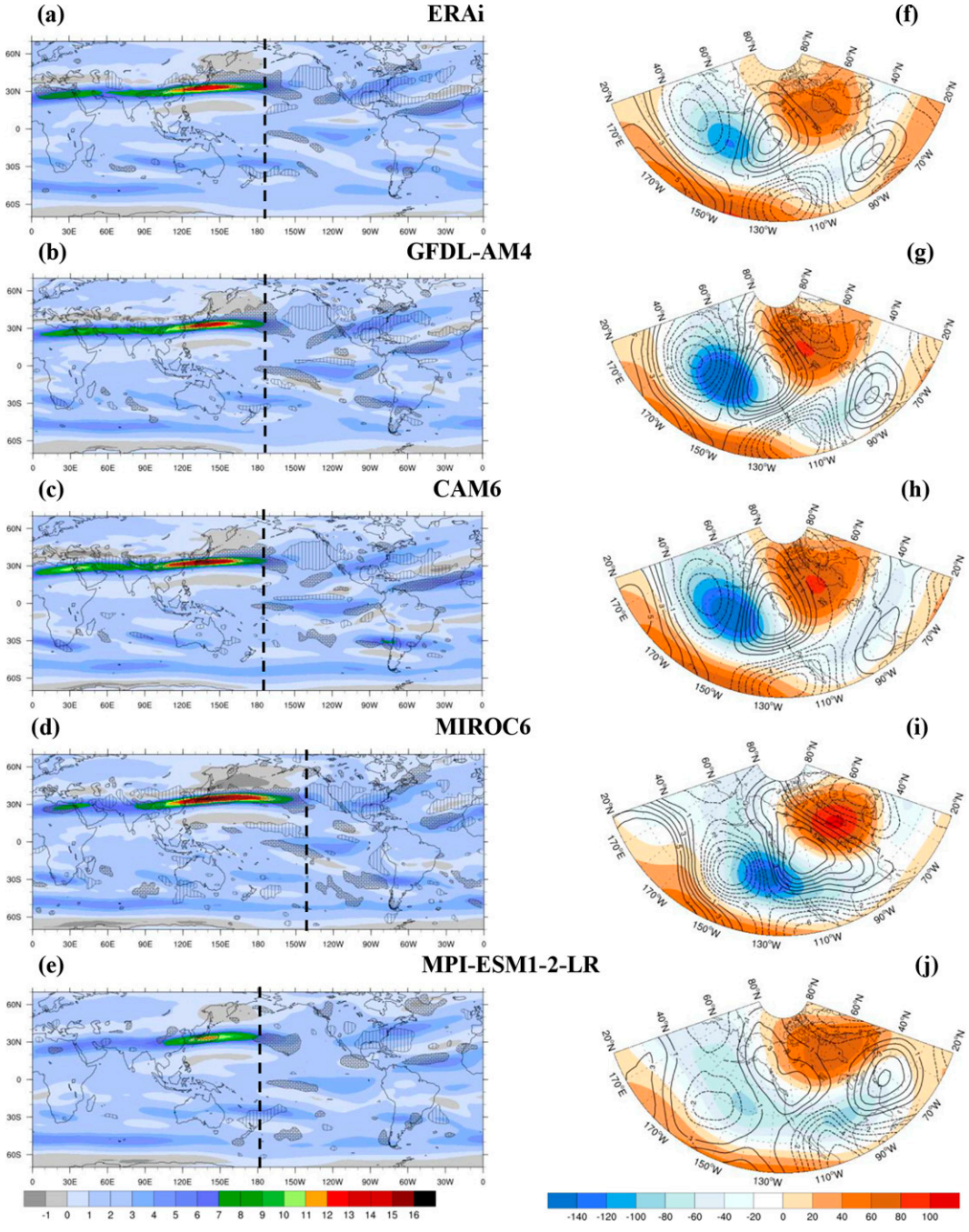

FIG. 11. 200-hPa boreal winter (DJF): (left) climatological β_* (shading; 10^{-11} m^{-1} s^{-1}) and RWS′ (dark hatching for positive values and light hatching for negative values; 10^{-11}s^{-2}); (right) 200-hPa geopotential height (shaded; m) and meridional wind (contours; m s^{-1}) anomalies during El Niño. Vertical lines in the left column correspond to longitude of zero values of β_* in North Pacific. Results from ERAi and a few AMIP6 models are shown.

Additionally, even for weaker RWS′ a realistic PNA/ENCI is simulated (e.g., ACCESS-ESM1-5). Generally, sensitivity of the two metrics is similar to both ENCI and PNA with one clear exception. Of all the AMIP6 models, MIROC6 represents the strongest RWS′ while the simulated PNA is the weakest, but ENCI appears realistic (Fig. 13f). A careful examination of contribution from all the four regions (Fig. 1a) indicate that due to unrealistic eastward extension of negative HGT200 over North Pacific and continental United States (Fig. 11i), contribution from the fourth region overwhelms, resulting in a realistic ENCI. Results presented in section 5 suggest that the two metrics are necessary but not sufficient conditions to represent a

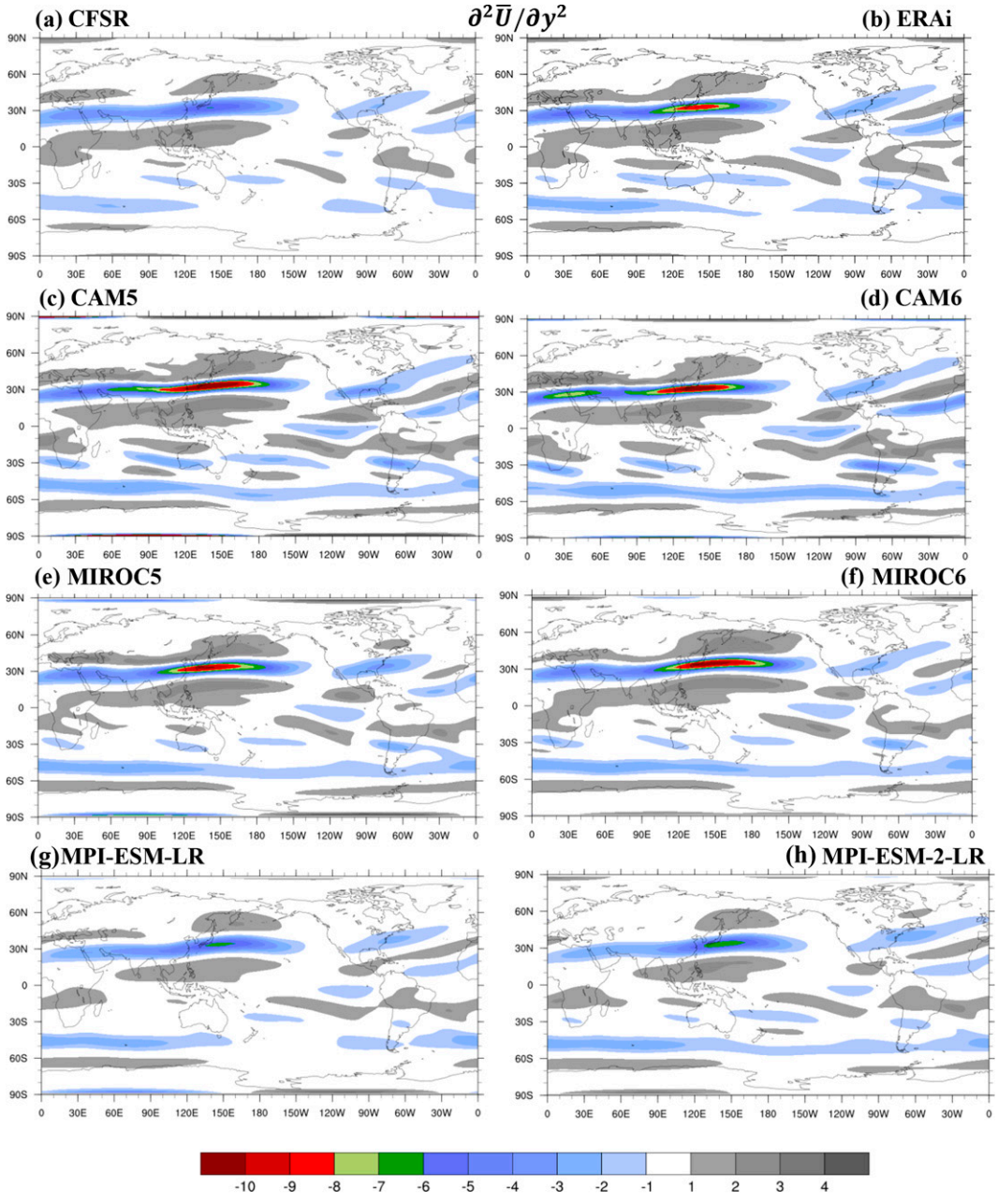

FIG. 12. Spatial maps of $\partial^2\overline{U}/\partial y^2$ (or local vorticity gradient) of the ambient zonal flow ($\overline{U}$) at 200 hPa. Results are from (a),(b) two reanalysis and (c)–(f) select AMIP5 (AMIP6) models are presented in the left (right) panels. Units are 10^{-11} m^{-1} s^{-1}.

realistic midlatitude circulation response during El Niño winters. More discussions on this aspect are provided below.

6. Model biases, improvements, and implications for model developers

a. *Quantification of model biases*

Figure 14 shows model biases (expressed in %) with respect to multireanalysis mean anomalies. AMIP5 (AMIP6) model biases are shown in the left (right) panels, and the key variables discussed in previous sections are shown. EPP wetness and MC-TWP dryness, in about two-thirds of all AMIP models, are weaker than observations. Irrespective of a model's ability to represent equatorial precipitation anomalies, biases in STNP convergence (and associated RWS′) are systematically weaker than in reanalysis. This implies a role for other processes in determining actual STNP convergence. In some models, the maximum level of anomalous divergence/convergence may not be at 200 hPa, an issue currently being investigated. As regards to β_*LON, biases in most models are

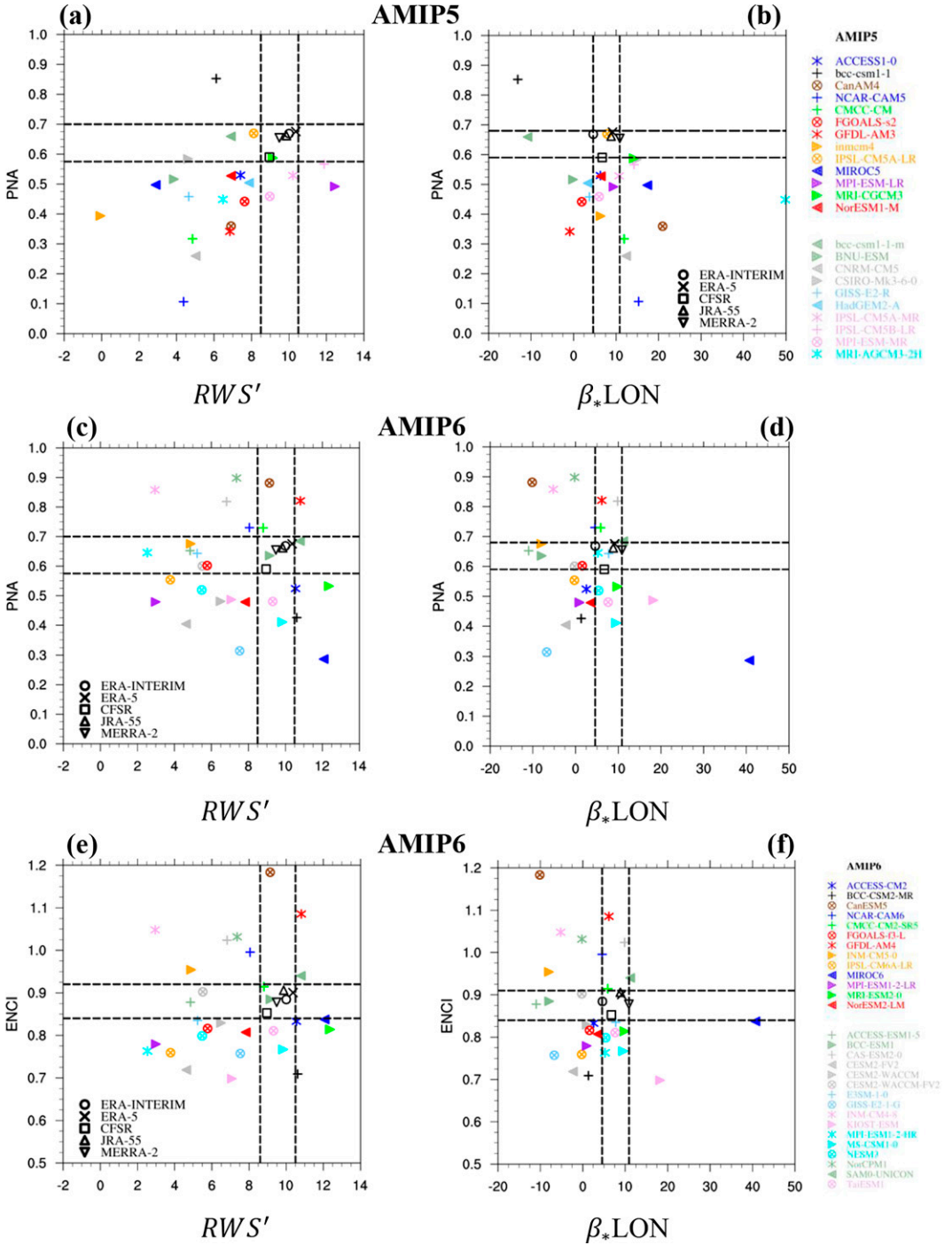

FIG. 13. (left) Scatterplots between RWS′ (10^{-11} s^{-2}) averaged over the STNP (25°–40°N, 150°E–160°W) and PNA; (right) scatterplots between β_*LON in the North Pacific and PNA. (a),(b) All AMIP5 models and (c),(d) all AMIP6 models. Scatterplot (e) between RWS′ and ENCI and (f) between β_*LON and ENCI in AMIP6 models. The vertical and horizontal dashed lines correspond to reanalysis uncertainties measured as lower and upper bound values among them, and a model simulation is interpreted to be realistic if its values fall within these uncertainties.

inclined toward being east of the date line in AMIP6 compared to west of the date line in AMIP5. In both AMIP versions, biases in both circulation indices are similar in any given model, suggesting model consistency in representing either of the two indices. In summary, model biases quantitatively range from (i) −55% to 40% for tropical precipitation, (ii) −80% to 20% for STNP convergence that directly impact primary RWS′ (−75% to 30%), and (iii) −60% to 40% for circulation response over the PNA region.

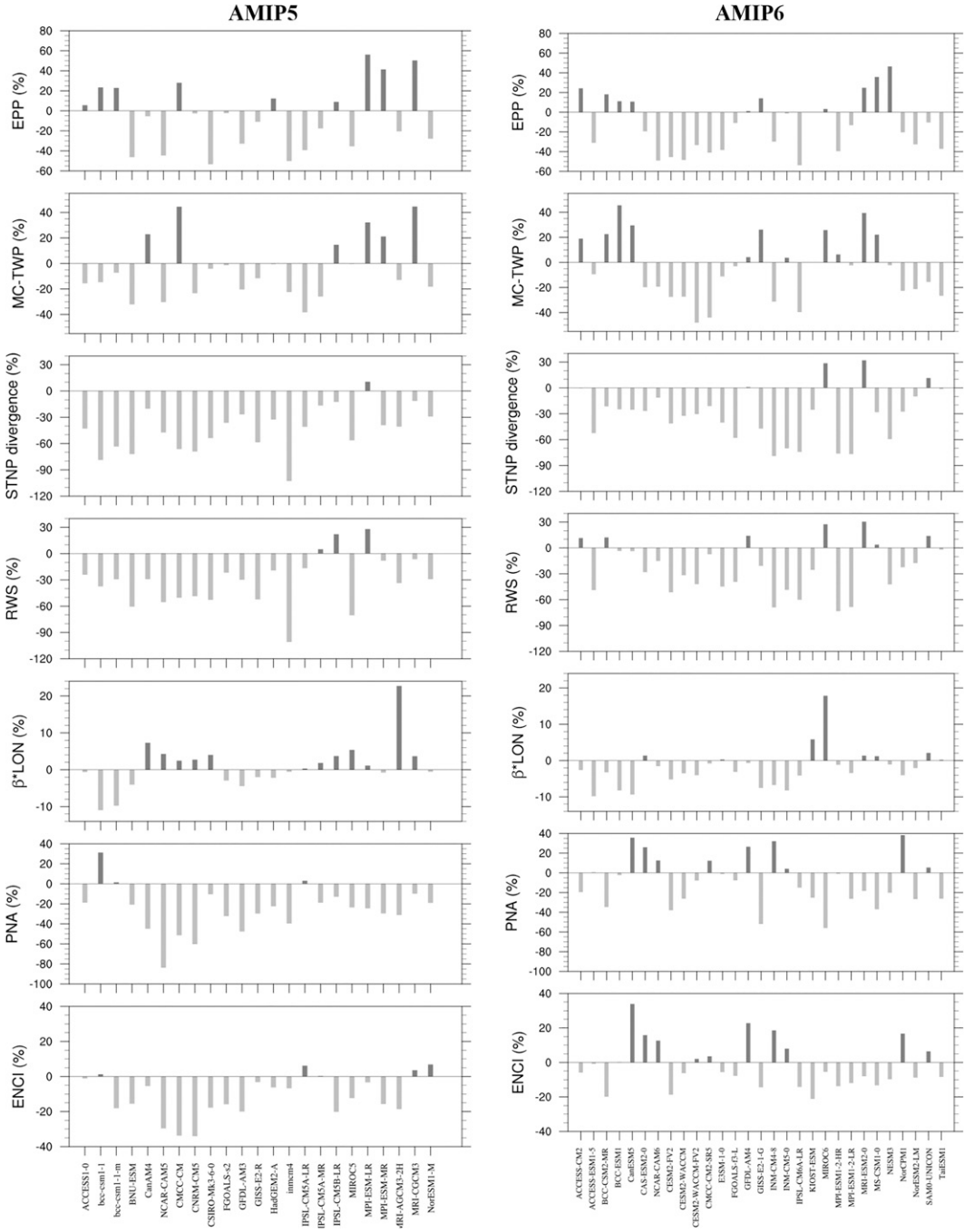

FIG. 14. (left) AMIP5 and (right) AMIP6 model biases with respect to multireanalysis (expressed in %). The variables are (first row) EPP, (second row) MC-TWP precipitation, (third row) STNP divergence at 200 hPa, (fourth row) RWS′ averaged over STNP, (fifth row) β_*LON in the central-North Pacific (0 values in β_*LON refers to date line), (sixth row) PNA, and (seventh row) ENCI indices.

b. *Improvements or degradations from AMIP5 to AMIP6*

Model results of the chain of processes presented above suggest that some of them are improved in AMIP6 and some are degraded. To highlight improvements for each modeling center, Fig. 15 shows results from models that participated in both AMIP versions. Here, biases are estimated with respect to their corresponding multireanalysis means. If the AMIP6 bias falls closer to reanalyses (boxed area in Fig. 15) compared to AMIP5 biases, it is interpreted as improved (left panels). Conversely, if the bias falls more distant, it is

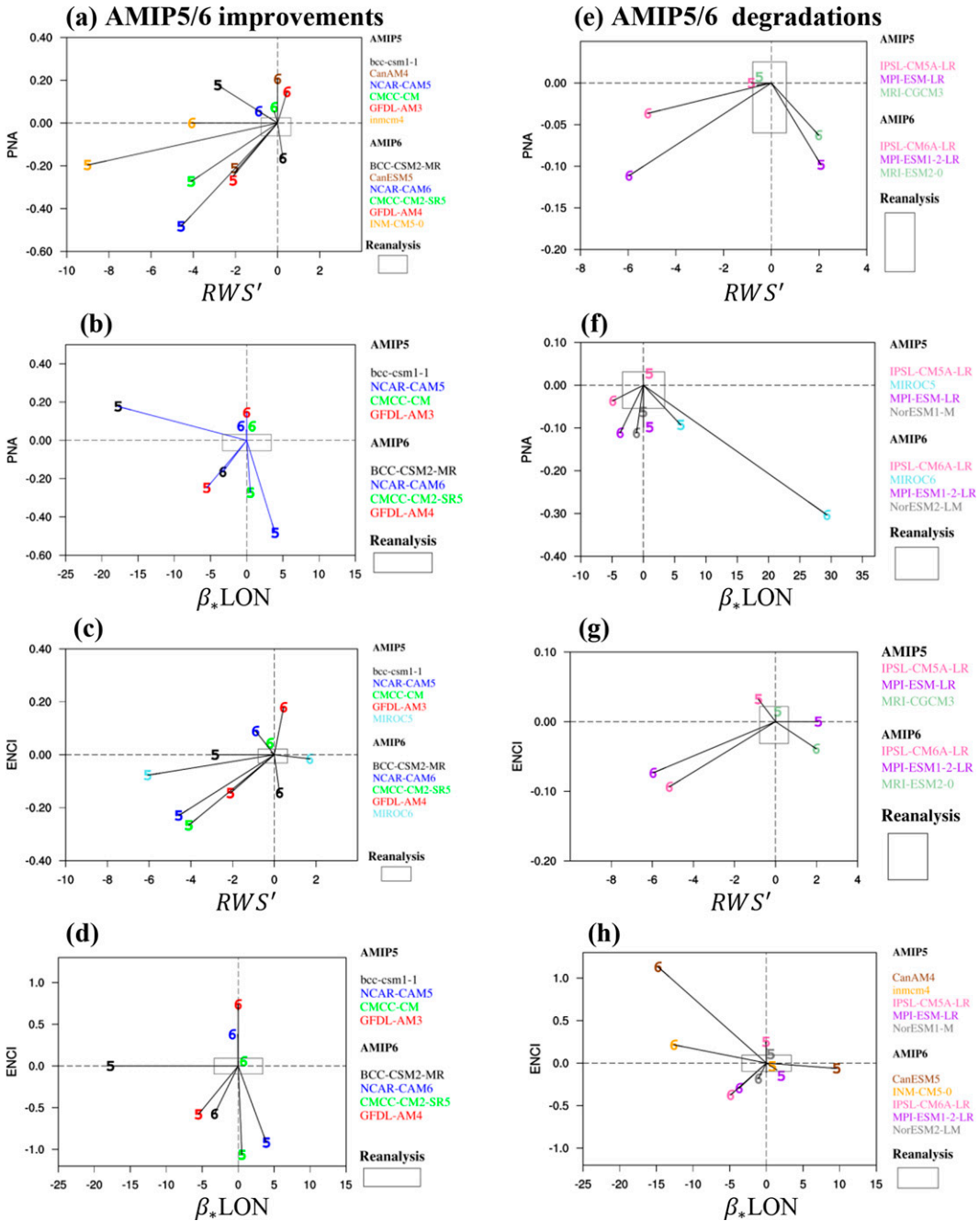

FIG. 15. Scatterplots to illustrate (a)–(d) improvements or (e)–(h) degradations in both variables in each panel from AMIP5 to AMIP6. Variables considered are RWS′ (10^{-11} s^{-2}) averaged over the STNP, β_*LON in the North Pacific, PNA and ENCI circulation indices. Model biases are estimated with respect to their corresponding multireanalysis means. (left) If the AMIP6 bias falls closer to reanalyses (boxed area) compared to AMIP5 biases, it is interpreted as improved. (right) Conversely, if the bias falls more distant, it is interpreted as degraded. In all panels, number 5 stands for AMIP5 and 6 refers to AMIP6, and colors correspond to the model's name. The 0 values in β_*LON refer to the date line.

interpreted as degraded (right panels). In all panels, number 5 stands for AMIP5 and 6 refers to AMIP6, and colors correspond to the model's name. If only one of the two variables in Fig. 15 is either improved or degraded, that model's results are not shown.

AMIP5 model values that lie in the bottom left quadrants (weak in both variables; Figs. 15a,c), and more eastward values of β_*LON (Figs. 15b,d) converge toward reanalysis values (boxed area) in AMIP6. These results convince us that there is an overall improvement in AMIP6 models' representations

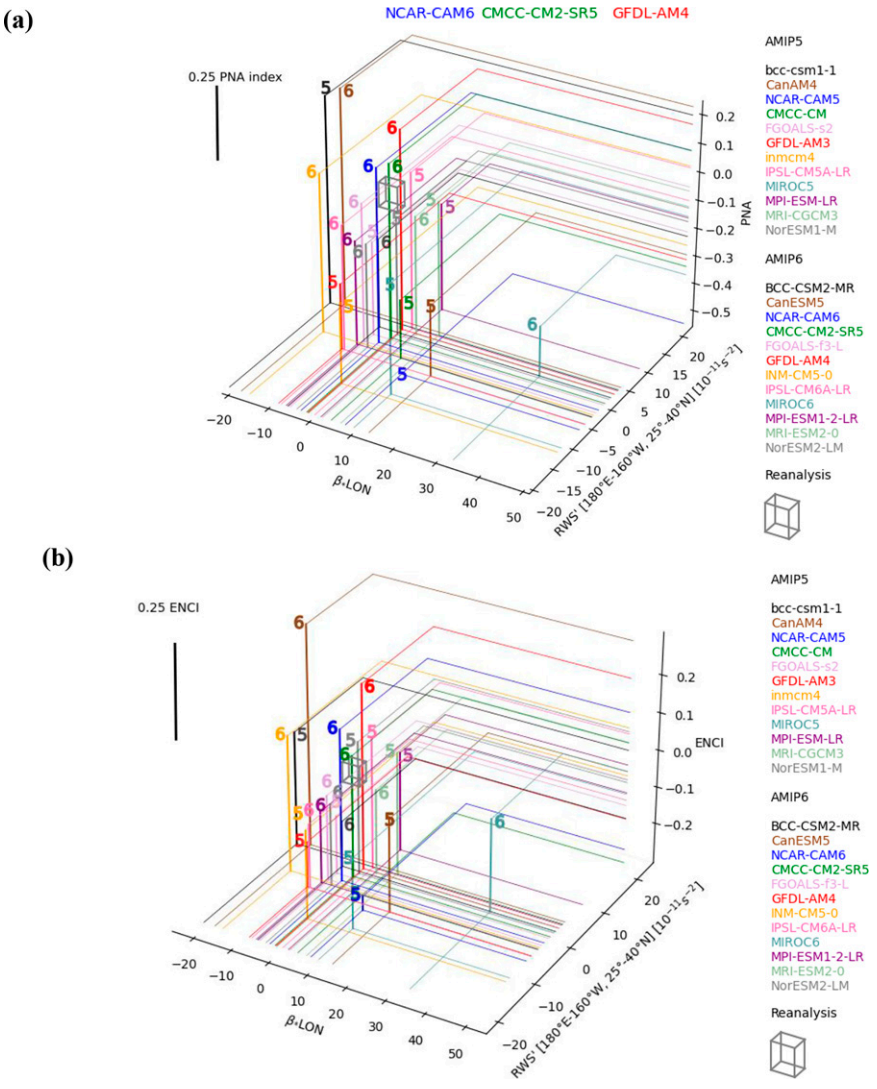

FIG. 16. Three-dimensional (3D) plots to highlight AMIP5/6 models representation of two metrics and their impact on (a) PNA and (b) ENCI indices. Independent variables are β_*LON in the North Pacific and RWS′ (10^{-11} s^{-2}) averaged over the STNP east of the date line (25°–40°N, 180°–160°W). Model biases are estimated with respect to their corresponding multireanalysis means. If the AMIP6 bias falls closer to reanalyses (boxed area) compared to AMIP5 biases, it is interpreted as improved. Conversely, if the bias falls more distant, it is interpreted as degraded. In all panels, number 5 stands for AMIP5 and 6 refers to AMIP6, and colors correspond to the model's name. Reference unit "line" represents 0.25 standard deviation. Models in which both metrics and PNA/ENCI indices improved are highlighted at the top.

of RWS′, β_*LON, PNA, and ENCI. In each of the panels, while the number of models showing improvements in both variables is different, four models show consistent improvements and they are BCC-CSM2-MR, NCAR-CAM6, GFDL-AM4, and CMCC-CM2-SR5. In these models, improved basic-state as evidenced by β_* (Figs. 15b,d) and representation of RWS′ (Figs. 5 and 6) in regions of lower K_s (Figs. 8 and 9), favor meridional propagation. While six models show improvements in RWS′ and PNA (Fig. 15a), β_*LON in CanESM5, for example, is positioned too westward of the date line (Fig. 13d), and an unrealistically strong PNA/ENCI is simulated. We offer possible reasons for these extremes in the appendix. It should be mentioned here that models that show improvements or degradations in RWS′ and PNA pair, or β_*LON and PNA pair, show similar results in RWS′ and ENCI pair, or β_*LON and ENCI pair.

In considering β_*LON and RWS′ as two independent metrics that collectively determine PNA/ENCI, we summarize their joint relationships in Fig. 16 with conventions used as in Fig. 15. In this cubic view, if both independent metrics are clustered around the reanalysis values (gray cubes), then height anomalies averaged over the PNA and ENCI are

realistic, and improvements in β_*LON and RWS′ and ENCI or PNA are readily apparent in their AMIP6 versions for the four models earlier identified in Fig. 15. Similarly, degradations in two models (IPSL-CM6A-LR and NorESM2-LM) are outliers. Furthermore, this plot suggests that if one of the two metrics is unrealistic so is the PNA/ENCI response. Figures 13 and 14 suggest that other AMIP6 models show realistic values either in RWS′ [e.g., Seoul National University Atmosphere Model, version 0, with a Unified Convection Scheme (SAM0-UNICON)] or β_*LON [e.g., Energy Exascale Earth System Model, version 1.0 (E3SM-1-0)] or both (e.g., TaiESM1). We discuss some aspects of these models' fidelity in the appendix.

c. *Implications for model developers*

In models, both in basic-state and anomalous conditions, changes in the response of moist processes either to parameterization modifications or tuning and calibration, can often change the nature of the seasonal distributions of tropical precipitation and heating, and by association moistening and divergence profiles. While validation of an integrated scalar quantity such as precipitation is mostly straightforward, an understanding of the circulation consequences in the tropics, and particularly the nonlinear wave–mean flow interactions of the extratropics is not. The intention would be to monitor simulation improvements over time. Equally, however, when inadvertent or unintended degradations are discovered, decisions need to be made on how to move forward. This could involve either a concerted effort to understand the processes leading to the degradation or accepting the response and moving forward regardless. By having a suite of PODs as an automated tool, a broad range of simulation features could be invoked that span the range of performance features for which a model is being designed. In the case of climate models this would include large-scale circulation features (the focus here), modes of variability and climate feedback processes (e.g., cloud feedbacks, precipitation, and temperatures). Thus, the assessment presented here is intended to provide useful feedback to model developers where POD performance changes can be linked to parameterization improvements, even though these linkages can often be circuitous and difficult to disentangle.

Model developers primarily focus on a very limited set of requirements or metrics in order to produce a useful model, often for CMIP (and also AMIP) purposes (Schmidt et al. 2017; Hourdin et al. 2017). The focus is often biased toward the larger climate change requirements, in order to capture historical, and therefore reliable, future evolution of a warming world, even though there is disagreement in priorities across the modeling centers. The analysis presented here is different, in that it captures a succession of processes critical to both climate change and Earth system prediction in the Northern Hemisphere, but it does so with a process-oriented focus that follows this succession from the tropical Pacific to the West Coast of the United States. Applying this particular POD continually through the development process will keep a regular check on the fidelity of the modeled response to anomalous El Niño convection (such a progression in coupled models is obviously a much greater challenge given the variation in Pacific SSTs and associated model biases). Applying a set of PODs is expected to reduce the frequent occurrence in model development of a particular process or mode of variability degrading over time. This degradation can be unknown to the developers earlier due to lack of availability of appropriate PODs. The hope is that it will become a standard method to assess models, in the same way that ENSO, the North Atlantic Oscillation (Simpson et al. 2020), and Madden–Julian oscillation (Chen et al. 2022) have become to date.

7. Conclusions

During boreal winters, to assess climate models' fidelity in representing ENSO-induced teleconnection over North Pacific and North America, as part of NOAA Model Diagnostics Task Force efforts, a process-oriented diagnostic (POD) package termed ENSO_RWS is developed. The POD assesses the chain of processes, that is, intermediate between equatorial Pacific precipitation (EPP) and the midlatitude circulation pattern that are rarely addressed in model development and evaluations. Ambient upper-tropospheric flow properties such as local vorticity gradient of the ambient zonal flow ($\partial^2\overline{U}/\partial y^2$), restoring force for Rossby waves (β_*), and stationary wavenumber (K_s) are estimated. The equivalent barotropic vorticity equation is then solved and the leading terms of RWS′ are quantified. For a realistic representation of the circulation response over the PNA regions, our working hypothesis is that models accurately represent the strength and location of primary RWS′, and spatial variations in $\partial^2\overline{U}/\partial y^2$ and β_*.

Our POD identifies two important metrics, and they are as follows:

- Spatial coherence in the primary RWS′ in the STNP.
- Spatial distributions in $\partial^2\overline{U}/\partial y^2$ and β_* to assess propagation of the radiated waves (β_*LON, i.e., zero values of β_* in the central North Pacific to the west or east of the date line).

Encouragingly, clear improvements in forcing (EPP) and response (STNP convergence) are noted in AMIP6 experiments leading to improvements in the simulation of primary RWS′ (Figs. 5 and 6) with subsequent improvements of β_*LON and PNA/ENCI (Figs. 15 and 16). If a model's fidelity in accurately representing spatially coherent negative β_* values over the western-central North Pacific (40°–60°N, 130°E–140°W) that depends on $\partial^2\overline{U}/\partial y^2$ is compromised, propagation characteristics of Rossby waves are impacted. If β_*LON lies well eastward, initial meridional propagation of Rossby waves from the forcing region are reflected. This results in zonally elongated height anomalies over central North Pacific with a weakened Aleutian low and PNA index (e.g., GFDL-AM3, CAM5). Conversely, if β_*LON lies well westward, multiple wave trains are simulated and constructive interference is postulated. This leads to a too strong of a PNA/ENCI (CanESM5, Fig. 13d), and further discussed in appendix.

Comparing models from the same modeling groups (Figs. 15 and 16), we note that if both the metrics are improved then

those models' representation of PNA and ENCI are most commonly improved, perhaps for correct reasons based on the interpretations offered here. Even in these models, however, need for improvements on other aspects such as arresting westward extension of enhanced EPP anomalies and associated zonally elongated RWS′ (e.g., CAM6) are brought out by the POD. If only one of the metrics is improved (e.g., RWS′ in MIROC6) and other metrics are worsened (β_* in MIROC6), our POD offers an explanation for the unrealistic spatial pattern and intensity in HGT200 over North Pacific (Fig. 11) and suggests which metrics need to be improved. Note that accurate estimation of RWS′ is dependent on divergent flow details that crucially depends on models' fidelity in accurately representing diabatic processes. Thus, the POD is expected to provide positive feedback to model developers where performance changes can be directly linked to parameterization changes, ultimately leading to improved model parameterizations. During the development process of a climate model, applying this POD continually will keep a regular check on the fidelity of the modeled response to anomalous El Niño convection in the presence of changing model ambient flow characteristics such as $\partial^2\overline{U}/\partial y^2$ and β_*.

Based on the lack of a one-to-one relationship between EPP and STNP convergence (Fig. 4), the suggestion is that the initial source of model error could very well lie in the vertical distribution of diabatic processes that largely determine divergent winds. A successive POD to assess vertical processes during ENSO is a logical next step and will be similarly applied to climate models.

Acknowledgments. The authors acknowledge the support from NOAA-MAPP Award NA18OAR4310279 for developing process-oriented diagnostics. We acknowledge the World Climate Research Programme's Working Group on Coupled Modelling, which is responsible for AMIP/CMIP, and we thank the climate modeling groups for producing and making available their model output. Authors sincerely acknowledge valuable comments from all the three anonymous reviewers that helped improve the manuscript. Critical comments from reviewer 3 were instrumental to improve the overall presentation of the manuscript. Dr. Neale also acknowledges the support by the U.S. Department of Energy, Office of Science, Office of Biological and Environmental Research (BER), Regional and Global Model Analysis (RGMA) component of the Earth and Environmental System Modeling Program under Award DE-SC0022070, and National Science Foundation (NSF) IA 1947282. This work was also supported by the National Center for Atmospheric Research (NCAR), which is a major facility sponsored by the NSF under Cooperative Agreement 1852977. This is IPRC Publication Number 1591 and SOEST Publication Number 11617.

Data availability statement. Data sets analyzed in the study include reanalysis data that are existing data products available at the locations cited in the respective references. Furthermore, standard model outputs that are archived as part of the CMIP6 are diagnosed, and the data are available at https://esgf-node.llnl.gov/search/cmip5/ and https://esgf-node.llnl.gov/search/cmip6/.

APPENDIX

Further Model Interpretations

For active model developers, the simulated circulation response in AMIP6 is too strong or weak or realistic, and do the two identified metrics, RWS′ and β_*LON, offer plausible explanations? In AMIP6, simulated circulation is realistic (e.g., ACCESS-ESM1-5, MPI-ESM1-2-HR, INM-CM5-0, BCC-ESM), and either too strong (e.g., CanESM5) or weak (e.g., ACCESS-CM2) in others. We further examined results from all the 28 AMIP6 models. While we do not discuss every model result in detail, we present a few that share common features, and offer possible interpretations.

While the simulated PNA/ENCI is realistic in some models, it may be for incorrect reasons. As an example, results from ACCESS-ESM1-5 (Figs. A1 and A2; bottom panels) show weakened Asian jet and weaker β_* along the jet, and spatially incoherent β_* (no negative β_* values between 30° and 50°N over western North Pacific and incorrect β_*LON), and more poleward orientation of upper-level divergence and RWS′ (~55°N). In this model, compared to reanalysis (Fig. 11f), positive HGT200 over north America is unrealistically strong and negative HGT200 over southeast United States is too weak, compensating for a realistic PNA/ENCI, and furthermore V200 shows more zonal characteristics over North Pacific and North America, indicative of errors in the wavy nature of the ambient flow.

For differing RWS′ strength, CanESM5, INM-CM-4-8, and NorCPM1 simulate PNA/ENCI values that are too strong (Figs. 13c,e). Are there common errors across these models? In all of them, β_*LON is positioned westward of the date line (Figs. 13d,f). As an example, Figs. A1 and A2 (top panels) show POD results for CanESM5. Of relevance, the ambient westerly Asian jet is diffused and weak, and consequently, $\partial^2\overline{U}/\partial y^2$ is too weak poleward of the jet maximum resulting in spatially contracted negative values of β_* to the west of the date line in the North Pacific. This, in conjunction with a reasonably positioned primary RWS′, meridional propagation of stationary Rossby waves is favored over *northwestern* Pacific and further poleward resulting in subtropical and high-latitude wave trains in CanESM5 (Fig. A1b). Thus, we speculate that due to constructive interferences of multiple waves, except the tropical one, the other three centers of action exhibit too-strong HGT200 values, resulting in an unrealistically strong PNA/ENCI (Fig. A1b).

On the other hand, simulated PNA/ENCI is weaker than reanalysis in about 50% of the AMIP6 models (Fig. 13). They are ACCESS-CM2, BCC-CSM2-MR, CESM-FV2, CESM2-WACCM, CESM2-WACCM-FV2, E3SM1.0, FGOALS-f3-L, GISS-E2-1-G, IPSL-CM6A-LR, SAM0-UNICON, MIROC6, MPI-ESM1-2-HR, MRI-ESM2-0, and Tai-ESM-1. This occurs despite both metrics being realistically represented in some of them (e.g., BCC-CSM2-MR and Tai-ESM-1). Common features in all these models include zonally elongated EPP, RWS′ and HGT200 over the North Pacific, radiation and propagation of multiple wave trains and spatially incoherent β_* variations (e.g., no negative values between 30° and 50°N over western North Pacific). To illustrate, we show results

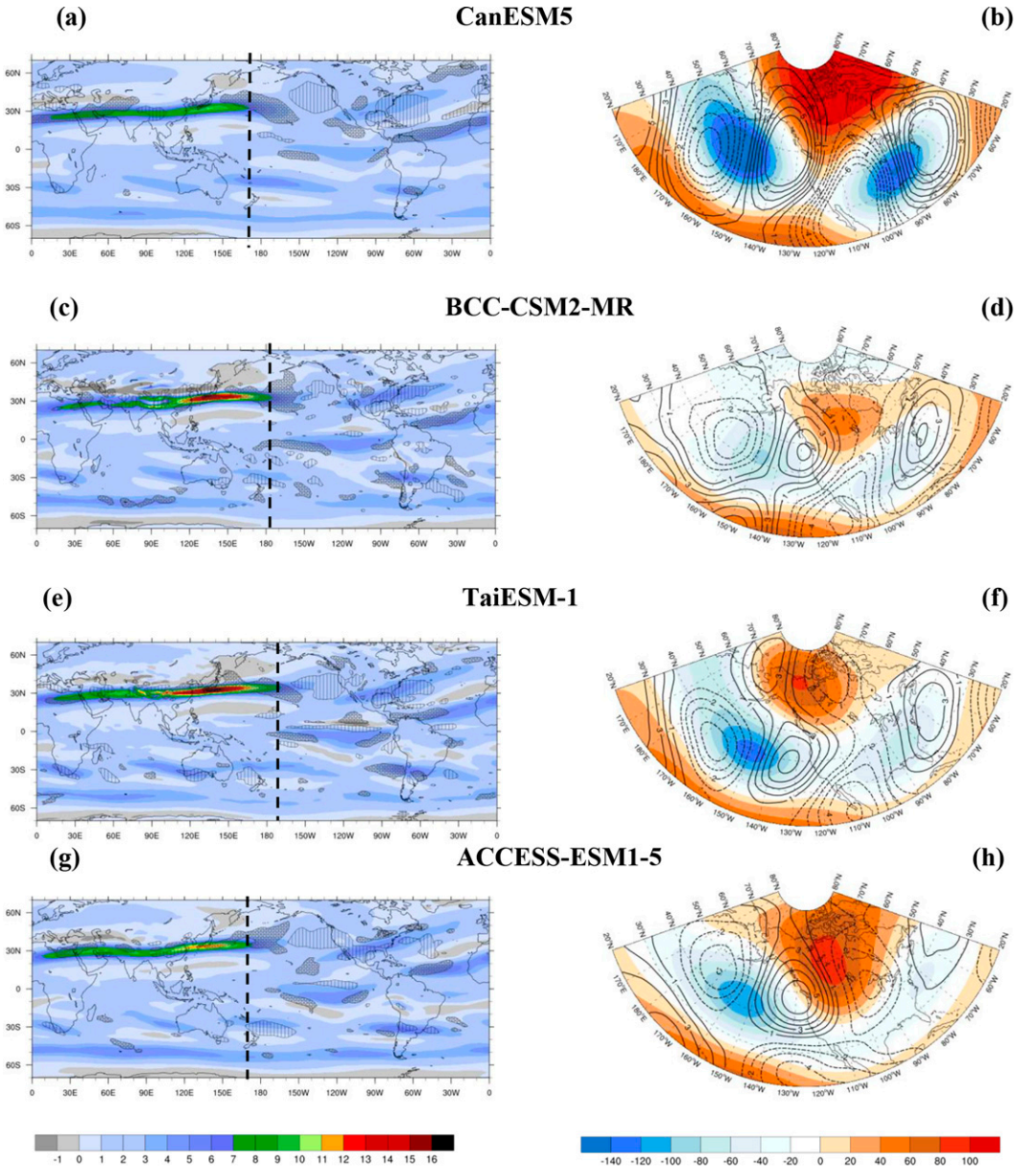

FIG. A1. 200-hPa boreal winter (DJF): (left) climatological β_* (shading; 10^{-11} m^{-1} s^{-1}) and total anomalous Rossby wave source (hatching for positive values and lines for negative values; 10^{-11} s^{-2}); (right) 200-hPa geopotential height (shaded; m) and meridional wind (contours; m s^{-1}) anomalies during El Niño. Vertical lines in the left column correspond to longitude of zero values of β_* in North Pacific (β_*LON). Results from a few AMIP6 models are shown.

(Figs. A1 and A2) from BCC-CSM2-MR (second row) and TaiESM-1 (third row).

In BCC-CSM2-MR, ambient flow properties are realistic but RWS′ is zonally elongated with signatures along the Asian jet and has a pronounced north–south orientation (reaching 55°–60°N) in central-North Pacific. HGT200 patterns are nearly circular over central-North Pacific (instead of elliptical as in reanalysis) and multiple wave trains are seen in the Northern Hemisphere. Annamalai et al. (2007) suggested that HGT200 due to short wavelength Rossby waves trapped by the jets, after exiting the jet region, are out-of-phase with HGT200 in the North Pacific with waves of longer wavelength (or lower K_s) forced by EPP-induced heating, and thus their destructive interference weakens PNA/ENCI. While results presented in Fig. 15 suggest an overall improvement from its AMIP5 version, caution needs to exercised based on the interpretations offered here. In TaiESM-1, EPP anomalies extend across the entire Pacific basin with consequences for zonally elongated primary RWS′ and HGT200 over the Aleutian region. Compared to

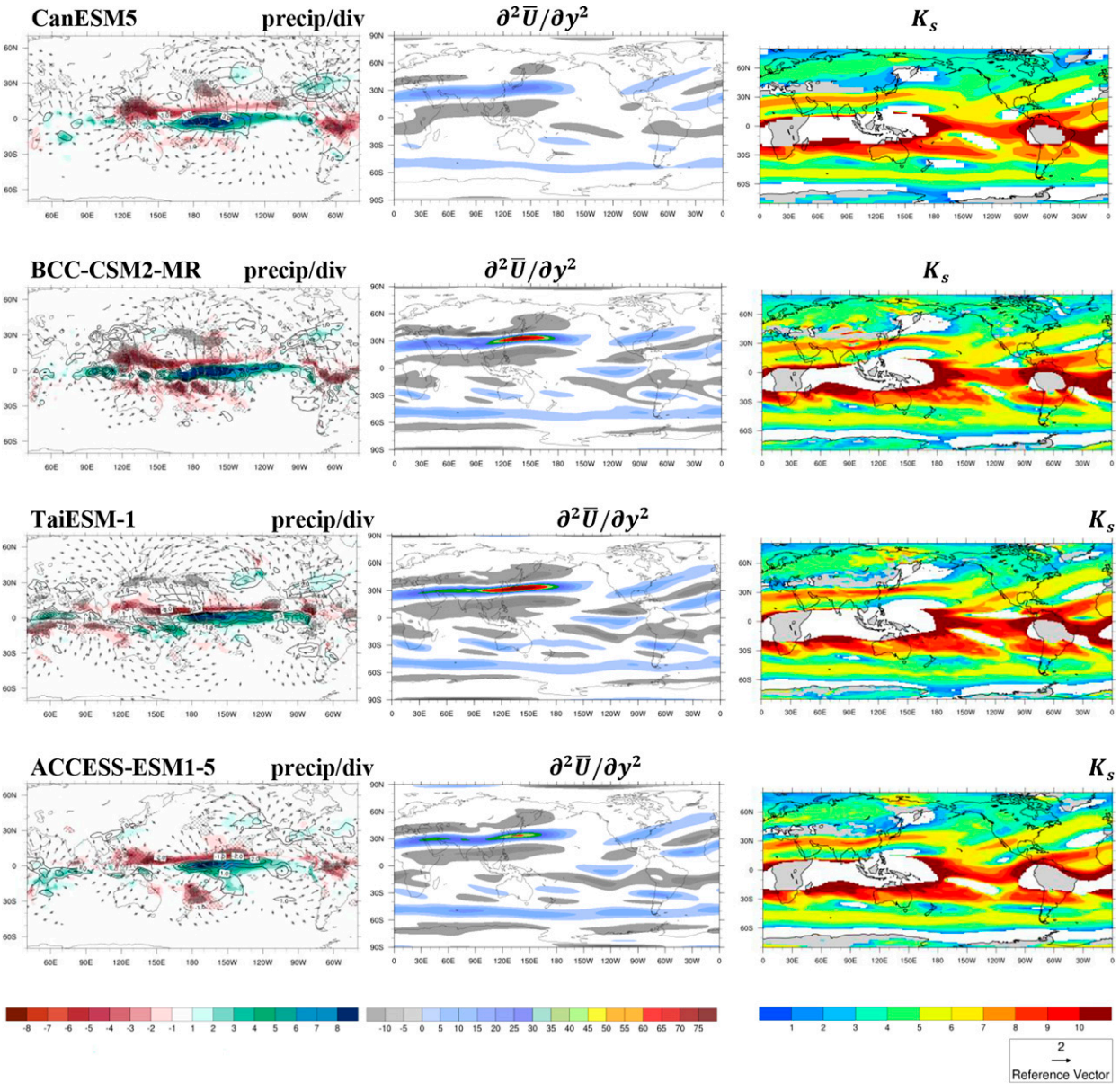

FIG. A2. Spatial maps of key variables during boreal winter (DJF) from a few models: (left) El Niño composite anomalous precipitation (mm day^{-1}; shaded), 200 hPa convergence/divergence (contours/hatching in units of 10^{-6} s^{-1}) and divergent wind (m s^{-1}; reference vector is shown); (center) $\partial^2\overline{U}/\partial y^2$ or meridional curvature of the ambient zonal flow ($\overline{U}$) at 200 hPa (10^{-11} m^{-1} s^{-1}); and (right) K_s, the stationary wavenumber. Models include (top to bottom) CanESM5, BCC-CSM2-MR, TaiESM-1, and ACCESS-ESM1-5.

reanalysis (Fig. 11b), two well-separated wave trains over North Pacific, one in midlatitudes (~40°N) and another in high latitudes (60°–70°N), are discernible.

Briefly, besides EPP forcing and ambient flow properties on planetary wave propagation, a number of other nonlinear processes are involved in accurately determining the magnitude of extratropical response. They include interactions with transients (e.g., storm-track changes; Held et al. 1989) and interference from midlatitude chaotic internal variability (Lau 1981), and horizontal and vertical distributions of diabatic heating anomalies over the tropical Indian Ocean region (Simmons et al. 1983; Ting and Sardeshmukh 1993; Lau 1997; Barsugli and Sardeshmukh 2002; Annamalai et al. 2007). In AGCMs, besides primary RWS′ in STNP, due to wave propagation new convergence and divergence centers can form leading to secondary RWS′ elsewhere (Figs. 5 and 6). Consequently, radiation of various wave trains with different wavelengths and great circle paths are expected. Therefore, a detailed assessment of all factors impacting PNA/ENCI amplitude is not feasible and is also beyond the scope of the present research.

REFERENCES

Annamalai, H., 2020: ENSO precipitation anomalies along the equatorial Pacific: Moist static energy framework diagnostics. *J. Climate*, **33**, 9103–9127, https://doi.org/10.1175/JCLI-D-19-0374.1.

——, J. M. Slingo, K. R. Sperber, and K. Hodges, 1999: The mean evolution and variability of the Asian summer monsoon: Comparison of ECMWF and NCEP/NCAR reanalyses. *Mon. Wea. Rev.*, **127**, 1157–1186, https://doi.org/10.1175/1520-0493(1999)127<1157:TMEAVO>2.0.CO;2.

——, P. Liu, and S.-P. Xie, 2005: Southwest Indian Ocean SST variability: Its local effect and remote influence on Asian monsoons. *J. Climate*, **18**, 4150–4167, https://doi.org/10.1175/JCLI3533.1.

——, H. Okajima, and M. Watanabe, 2007: Possible impact of Indian Ocean SST on the Northern Hemisphere circulation during El Niño. *J. Climate*, **20**, 3164–3189, https://doi.org/10.1175/JCLI4156.1.

Barsugli, J. J., and P. D. Sardeshmukh, 2002: Global atmospheric sensitivity to tropical SST anomalies throughout the Indo-Pacific basin. *J. Climate*, **15**, 3427–3442, https://doi.org/10.1175/1520-0442(2002)015<3427:GASTTS>2.0.CO;2.

Branstator, G. W., 1983: Horizontal energy propagation in a baroclinic atmosphere with meridional and zonal structure. *J. Atmos. Sci.*, **40**, 1689–1708, https://doi.org/10.1175/1520-0469(1983)040<1689:HEPIAB>2.0.CO;2.

——, 1985: Analysis of general circulation model sea-surface temperature anomaly experiments using a linear model. Part I: Forced solutions. *J. Atmos. Sci.*, **42**, 2225–2241, https://doi.org/10.1175/1520-0469(1985)042<2225:AOGCMS>2.0.CO;2.

Chen, G., J. Ling, R. Zhang, Z. Xiao, and C. Li, 2022: The MJO from CMIP5 to CMIP6: Perspectives from tracking MJO precipitation. *Geophys. Res. Lett.*, **49**, e2021GL095241, https://doi.org/10.1029/2021GL095241.

Dee, D. P., and Coauthors, 2011: The ERA-Interim reanalysis: Configuration and performance of the data assimilation system. *Quart. J. Roy. Meteor. Soc.*, **137**, 553–597, https://doi.org/10.1002/qj.828.

Deser, C., L. Terray, and A. S. Phillips, 2016: Forced and internal components of winter air temperature trends over North America during the past 50 years: Mechanisms and implications. *J. Climate*, **29**, 2237–2258, https://doi.org/10.1175/JCLI-D-15-0304.1.

Di Carlo, E., and P. Ruggieri, P. Davini, S. Tibaldi and S. Corti, 2022: ENSO teleconnections and atmospheric mean state in idealised simulations. *Climate Dyn.*, **59**, 3287–3304, https://doi.org/10.1007/s00382-022-06261-w.

Eyring, V., S. Bony, G. A. Meehl, C. A. Senior, B. Stevens, R. J. Stouffer, and K. E. Taylor, 2016: Overview of the Coupled Model Intercomparison Project phase 6 (CMIP6) experimental design and organization. *Geosci. Model Dev.*, **9**, 1937–1958, https://doi.org/10.5194/gmd-9-1937-2016.

Gates, W. L., 1992: AMIP: The Atmospheric Model Intercomparison Project. *Bull. Amer. Meteor. Soc.*, **73**, 1962–1970, https://doi.org/10.1175/1520-0477(1992)073<1962:ATAMIP>2.0.CO;2.

Gelaro, R., and Coauthors, 2017: The Modern-Era Retrospective Analysis for Research and Applications, version 2 (MERRA-2). *J. Climate*, **30**, 5419–5454, https://doi.org/10.1175/JCLI-D-16-0758.1.

Held, I. M., and I.-S. Kang, 1987: Barotropic models of the extratropical response to El Niño. *J. Atmos. Sci.*, **44**, 3576–3586, https://doi.org/10.1175/1520-0469(1987)044<3576:BMOTER>2.0.CO;2.

——, S. W. Lyons, and S. Nigam, 1989: Transients and the extratropical response to El Niño. *J. Atmos. Sci.*, **46**, 163–174, https://doi.org/10.1175/1520-0469(1989)046<0163:TATERT>2.0.CO;2.

Herbasch, H., and Coauthors, 2020: ERA5 global reanalysis. *Quart. J. Roy. Meteor. Soc.*, **146**, 1999–2049, https://doi.org/10.1002/qj.3803.

Hoerling, M. P., and A. Kumar, 2002: Atmospheric response patterns associated with tropical forcing. *J. Climate*, **15**, 2184–2203, https://doi.org/10.1175/1520-0442(2002)015<2184:ARPAWT>2.0.CO;2.

——, ——, and M. Zhong, 1997: El Niño, La Niña, and the nonlinearity of their teleconnections. *J. Climate*, **10**, 1769–1786, https://doi.org/10.1175/1520-0442(1997)010<1769:ENOLNA>2.0.CO;2.

Horel, J. D., and J. M. Wallace, 1981: Planetary-scale atmospheric phenomena associated with the Southern Oscillation. *Mon. Wea. Rev.*, **109**, 813–829, https://doi.org/10.1175/1520-0493(1981)109<0813:PSAPAW>2.0.CO;2.

Hoskins, B. J., and D. J. Karoly, 1981: The steady linear response of a spherical atmosphere to thermal and orographic forcing. *J. Atmos. Sci.*, **38**, 1179–1196, https://doi.org/10.1175/1520-0469(1981)038<1179:TSLROA>2.0.CO;2.

——, and T. Ambrizzi, 1993: Rossby wave propagation in a realistic longitudinally varying flow. *J. Atmos. Sci.*, **50**, 1661–1671, https://doi.org/10.1175/1520-0469(1993)050<1661:RWPOAR>2.0.CO;2.

——, A. J. Simmons, and D. G. Andrews, 1977: Energy dispersion in a barotropic atmosphere. *Quart. J. Roy. Meteor. Soc.*, **103**, 553–567, https://doi.org/10.1002/qj.49710343802.

Hourdin, F., and Coauthors, 2017: The art and science of climate model tuning. *Bull. Amer. Meteor. Soc.*, **98**, 589–602, https://doi.org/10.1175/BAMS-D-15-00135.1.

Jin, F., and B. J. Hoskins, 1995: The direct response to tropical heating in a baroclinic atmosphere. *J. Atmos. Sci.*, **52**, 307–319, https://doi.org/10.1175/1520-0469(1995)052<0307:TDRTTH>2.0.CO;2.

Kang, I.-S., and I. M. Held, 1986: Linear and nonlinear diagnostic models of stationary eddies in the upper troposphere during northern summer. *J. Atmos. Sci.*, **43**, 3045–3057, https://doi.org/10.1175/1520-0469(1986)043<3045:LANDMO>2.0.CO;2.

Kobayashi, S., and Coauthors, 2015: The JRA-55 reanalysis: General specifications and basic characteristics. *J. Meteor. Soc. Japan*, **93**, 5–48, https://doi.org/10.2151/jmsj.2015-001.

Kumar, A., and M. P. Hoerling, 1995: Prospects and limitations of seasonal atmospheric GCM predictions. *Bull. Amer. Meteor. Soc.*, **76**, 335–345, https://doi.org/10.1175/1520-0477(1995)076<0335:PALOSA>2.0.CO;2.

——, and ——, 1997: Interpretation and implications of the observed inter-El Niño variability. *J. Climate*, **10**, 83–91, https://doi.org/10.1175/1520-0442(1997)010<0083:IAIOTO>2.0.CO;2.

——, Q. Zhang, P. Peng, and B. Jha, 2005: SST-forced atmospheric variability in an atmospheric general circulation model. *J. Climate*, **18**, 3953–3967, https://doi.org/10.1175/JCLI3483.1.

Lau, N.-C., 1981: A diagnostic study of recurrent meteorological anomalies appearing in a 15-year simulation with a GFDL general circulation model. *Mon. Wea. Rev.*, **109**, 2287–2311, https://doi.org/10.1175/1520-0493(1981)109<2287:ADSORM>2.0.CO;2.

——, 1997: Interactions between global SST anomalies and the midlatitude atmospheric circulation. *Bull. Amer. Meteor. Soc.*, **78**, 21–34, https://doi.org/10.1175/1520-0477(1997)078<0021:IBGSAA>2.0.CO;2.

——, and M. J. Nath, 1994: A modeling study of the relative roles of tropical and extratropical SST anomalies in the variability of the global atmosphere–ocean system. *J. Climate*, **7**, 1184–1207, https://doi.org/10.1175/1520-0442(1994)007<1184:AMSOTR>2.0.CO;2.

Li, R. K. K., T. Woollings, C. O'Reilly, and A. A. Scaife, 2020: Effect of the North Pacific tropospheric waveguide on the fidelity of model El Niño teleconnections. *J. Climate*, **33**, 5223–5237, https://doi.org/10.1175/JCLI-D-19-0156.1.

Lopez, H., and B. Kirtman, 2019: ENSO influence over the Pacific North American sector: Uncertainty due to atmospheric internal variability. *Climate Dyn.*, **52**, 6149–6172, https://doi.org/10.1007/s00382-018-4500-0.

Maloney, E. D., and Coauthors, 2019: Process-oriented evaluation of climate and weather forecasting models. *Bull. Amer. Meteor. Soc.*, **100**, 1665–1686, https://doi.org/10.1175/BAMS-D-18-0042.1.

Palmer, T. N., and D. A. Mansfield, 1986: A study of wintertime circulation anomalies during past El Niño events using a high resolution general circulation model. I: Influence of model climatology. *Quart. J. Roy. Meteor. Soc.*, **112**, 613–638, https://doi.org/10.1002/qj.49711247304.

Peng, P., and A. Kumar, 2005: A large ensemble analysis of the influence of tropical SSTs on seasonal atmospheric variability. *J. Climate*, **18**, 1068–1085, https://doi.org/10.1175/JCLI-3314.1.

——, ——, and B. Jha, 2014: Climate mean, variability and dominant patterns of the Northern Hemisphere wintertime mean atmospheric circulation in the NCEP CFSv2. *Climate Dyn.*, **42**, 2783–2799, https://doi.org/10.1007/s00382-014-2116-6.

Rasmusson, E. M., and T. H. Carpenter, 1982: Variations in tropical sea surface temperature and surface wind fields associated with the Southern Oscillation/El Niño. *Mon. Wea. Rev.*, **110**, 354–384, https://doi.org/10.1175/1520-0493(1982)110<0354:VITSST>2.0.CO;2.

Saha, S. S., and Coauthors, 2010: The NCEP Climate Forecast System reanalysis. *Bull. Amer. Meteor. Soc.*, **91**, 1015–1058, https://doi.org/10.1175/2010BAMS3001.1.

Sardeshmukh, P. D., and B. J. Hoskins, 1988: The generation of global rotational flow by steady idealized tropical divergence. *J. Atmos. Sci.*, **45**, 1228–1251, https://doi.org/10.1175/1520-0469(1988)045<1228:TGOGRF>2.0.CO;2.

Schmidt, G. A., and Coauthors, 2017: Practice and philosophy of climate model tuning across six US modeling centers. *Geosci. Model Dev.*, **10**, 3207–3223, https://doi.org/10.5194/gmd-10-3207-2017.

Shukla, J., and J. M. Wallace, 1983: Numerical simulation of the atmospheric response to equatorial Pacific sea surface temperature anomalies. *J. Atmos. Sci.*, **40**, 1613–1630, https://doi.org/10.1175/1520-0469(1983)040<1613:NSOTAR>2.0.CO;2.

——, and Coauthors, 2000: Dynamical seasonal prediction. *Bull. Amer. Meteor. Soc.*, **81**, 2593–2606, https://doi.org/10.1175/1520-0477(2000)081<2593:DSP>2.3.CO;2.

Simmons, A. J., J. M. Wallace, and G. W. Branstator, 1983: Barotropic wave propagation, and instability, and atmospheric teleconnections. *J. Atmos. Sci.*, **40**, 1363–1392, https://doi.org/10.1175/1520-0469(1983)040<1363:BWPAIA>2.0.CO;2.

Simpson, I. R., and Coauthors, 2020: An evaluation of the large-scale atmospheric circulation and its variability in CESM2 and other CMIP models. *J. Geophys. Res. Atmos.*, **125**, e2020JD032835, https://doi.org/10.1029/2020JD032835.

Straus, D. M., and J. Shukla, 2002: Does ENSO force the PNA? *J. Climate*, **15**, 2340–2358, https://doi.org/10.1175/1520-0442(2002)015<2340:DEFTP>2.0.CO;2.

Ting, M., and P. D. Sardeshmukh, 1993: Factors determining the extratropical response to equatorial diabatic heating anomalies. *J. Atmos. Sci.*, **50**, 907–918, https://doi.org/10.1175/1520-0469(1993)050<0907:FDTERT>2.0.CO;2.

Trenberth, K. E., G. W. Branstator, D. Karoly, A. Kumar, N.-C. Lau, and C. Ropelewski, 1998: Progress during TOGA in understanding and modeling global teleconnections associated with tropical sea surface temperatures. *J. Geophys. Res.*, **103**, 14 291–14 324, https://doi.org/10.1029/97JC01444.

Wallace, J. M., and D. S. Gutzler, 1981: Teleconnections in geopotential height field during the Northern Hemisphere winter. *Mon. Wea. Rev.*, **109**, 784–812, https://doi.org/10.1175/1520-0493(1981)109<0784:TITGHF>2.0.CO;2.

——, E. M. Rasmusson, T. P. Mitchell, V. E. Kousky, E. S. Sarachik, and H. von Storch, 1998: On the structure and evolution of ENSO-related climate variability in the tropical Pacific: Lessons from TOGA. *J. Geophys. Res.*, **103**, 14 241–14 259, https://doi.org/10.1029/97JC02905.

Zhang, C., D. S. Nolan, C. D. Thorncroft, and H. Nguyen, 2008: Shallow meridional circulations in the tropical atmosphere. *J. Climate*, **21**, 3453–3470, https://doi.org/10.1175/2007JCLI1870.1.